



# Direct numerical simulation of turbulent flow and structures in a circular pipe subjected to axial system rotation

Zhao-Ping Zhang<sup>1</sup> and Bing-Chen Wang<sup>1,†</sup>

<sup>1</sup>Department of Mechanical Engineering, University of Manitoba, Winnipeg, MB R3T 5V6, Canada

(Received 14 July 2023; revised 21 July 2024; accepted 22 July 2024)

Turbulent circular pipe flows subjected to axial system rotation are studied using direct numerical simulations (DNS) for a wide range of rotation numbers of  $Ro_b = 0-20$  at a fixed Reynolds number. To ensure that energetic turbulent eddy motions are captured at high rotation numbers, long pipes up to  $L_z = 180\pi R$  are used in DNS. Two types of energy-containing flow structures have been observed. The first type is hairpin structures that are characteristic of the turbulent boundary layer developing over the pipe wall for both non-rotating and axially rotating flows. The second type is Taylor columns forming at moderate and high rotation numbers. Based on the study of two-point autocorrelation coefficients, it is observed that Taylor columns exhibit quasi-periods in both axial and azimuthal directions. According to the premultiplied spectra, Taylor columns feature one single characteristic axial length scale at the moderate rotation numbers but two at high rotation numbers. It is discovered that the axial system rotation suppresses the sweep events systematically and impedes the formation of hairpin structures. As the rotation number is increased, the turbulence kinetic energy held by Taylor columns enhances rapidly associated with significant increases in their axial length scales.

**Key words:** pipe flow, rotating turbulence, turbulence simulation

## 1. Introduction

Turbulent flow within a circular pipe subjected to system rotation represents an interesting topic with important applications in areas such as internal blade cooling of gas turbines and rotary machines. The system rotation of the circular pipe may occur either radially about a diameter of the pipe, or axially about the centreline of the pipe. In response to either radial or axial system rotation, Coriolis force is induced which acts upon the fluid flow to dramatically alter the turbulence statistics and coherent structures. As is

† Email address for correspondence: [BingChen.Wang@Umanitoba.Ca](mailto:BingChen.Wang@Umanitoba.Ca)

well known, turbulent flow through a stationary (non-rotating) circular pipe is a classical research subject, which has been extensively studied using direct numerical simulations (DNS) by Eggels *et al.* (1994), Wu & Moin (2008), Chin *et al.* (2010) and Wu, Baltzer & Adrian (2012). By contrast, the number of DNS studies on either radially or axially rotating circular pipe flows is still very limited in the literature. Recently, Zhang & Wang (2019) carried out a DNS study of turbulent flow in a circular pipe subjected to radial system rotation and observed secondary flows appearing as streamwise-elongated large-scale counter-rotating vortices. Following our previous DNS study of radially rotating pipe flows (Zhang & Wang 2019), here we extend the research to DNS of axially rotating pipe flows. The physical mechanisms of circular pipe flows under the radial and axial system rotations are drastically different due to the differences in the direction of the Coriolis force. In the following, we concentrate on reviewing the literature of turbulent flows subjected to streamwise (or axial) system rotation. To establish a broader understanding of the subject, we begin with reviewing experimental and numerical studies of streamwise-rotating plane-channel flows and rotating isotropic turbulence and, then, focus on reviewing literature about axially rotating circular pipe flows.

### 1.1. *Flow structures in streamwise-rotating channel and rotating isotropic turbulence*

A streamwise-rotating plane-channel flow is similar to an axially rotating circular pipe flow in the sense that the direction and effects of the Coriolis force induced by the system rotation share certain common features, which are fundamentally different from those of spanwise-rotating plane-channel flows (Kristoffersen & Andersson 1993; Pallares & Davidson 2000; Wu & Kasagi 2004; Grundestam, Wallin & Johansson 2008; Wallin, Grundestam & Johansson 2013; Xia, Shi & Chen 2016) and radially rotating duct or circular pipe flows (Fang *et al.* 2017; Zhang & Wang 2019). Furthermore, compared with an axially rotating circular pipe flow, a streamwise-rotating turbulent Poiseuille flow confined in a plane channel is free from any domain curvature effects.

The effects of streamwise system rotation on turbulent plane-channel flow and structures under different Reynolds numbers and rotation numbers were studied using DNS by Weller & Oberlack (2006*a,b*). They observed that the mean spanwise velocity profile changes its direction three times between the two planes, showing an interesting ‘(double) S-shaped triple-zero-crossing pattern’ in the mean secondary flow in the cross-stream plane. These research findings are further confirmed by Oberlack *et al.* (2006) through an analytical study based on the group theory and by Recktenwald *et al.* (2007) and Recktenwald, Alkishriwi & Schröder (2009) through a study based on both large-eddy simulations (LES) and a particle image velocimetry (PIV) experiment. Based on their analytical and DNS studies, Yang, Su & Wu (2010) investigated the characteristics of the flow field of a streamwise-rotating plane-channel flow using a helical-wave decomposition method. Through analyses of their DNS data, they observed inertial waves and large tilted coherent structures along the streamwise direction.

Recently, Yang & Wang (2018) performed DNS to study streamwise-rotating channel flow at high rotation numbers. In order to capture the streamwise-elongated turbulence structures, a very long streamwise domain of  $512\pi\delta$  was used in their DNS, where  $\delta$  is the half-channel height. The influence of streamwise system rotation on the size, strength and characteristic wavelength of the streamwise-elongated turbulence structures was later refined by Yang *et al.* (2018) through a study of the modulating effects of streamwise system rotation on both the amplitude and wavenumber of pressure fluctuations. To achieve this goal, the pressure field was decomposed into a rotation-induced component and a

convection-induced component. Yu *et al.* (2022) conducted DNS of streamwise-rotating plane-channel flows and focused their study on turbulent transport of helicity under the influence of Coriolis force in both physical and spectral spaces. They observed that in contrast to the canonical test case of a stationary turbulent channel flow, the appearance of high helicity in a streamwise-rotating plane-channel flow mainly originates from the mean secondary flows, and it manifests as the mean spanwise velocity and streamwise vorticity.

The streamwise elongated turbulence structures observed in Yang & Wang (2018) can be well explained by the classical Taylor–Proudman theorem of the inviscid flow theory and relate to ‘Taylor columns’ that have been studied extensively in the literature of rotating isotropic turbulence. According to the Taylor–Proudman theorem, the velocity field of a rotating inviscid flow (at an angular speed  $\Omega_z$ ) is invariant along the rotation axis ( $z$ ), i.e.  $\partial \mathbf{u} / \partial z = \mathbf{0}$ . This further facilitates the formation of Taylor columns, which are two-dimensional (2-D) ‘cyclonic’ or ‘columnar’ flow structures along the rotating axis (Bartello, Métais & Lesieur 1994; Yoshimatsu, Midorikawa & Kaneda 2011; Pestana & Hickel 2020). The presence of Taylor columns has been widely observed in viscous flows in Earth’s atmospheres and oceans, and in DNS studies of forced isotropic turbulence (see, e.g., Smith & Waleffe 1999; Gallet 2015; Buzzicotti *et al.* 2018; van Kan & Alexakis 2020; Pestana & Hickel 2020) and decaying isotropic turbulence (see, e.g., Staplehurst & Davidson 2008; Thiele & Müller 2009; Yoshimatsu *et al.* 2011). According to Bartello *et al.* (1994) and van Kan & Alexakis (2020), in the context of isotropic turbulence, the system rotation tends to suppress variations of the flow motion along the axis of rotation which facilitates formation of quasi-2-D Taylor columns at high rotation numbers (or low Rossby numbers).

### 1.2. Axially rotating pipe flows

In comparison with the streamwise-rotating plane-channel flows as reviewed previously, the presence of circumferential curvature imposes additional complexity to the secondary-flow structures in an axially rotating circular pipe flow. In their pioneering work, Murakami & Kikuyama (1980) conducted an experiment to investigate the effects of axial system rotation on a turbulent pipe flow and observed that turbulence level of the flow was suppressed as the rotation number rose. Experimental measurements of axially rotating pipe flows were also conducted using hotwires by Kikuyama, Murakami & Nishibori (1983*a*), three-hole pressure probes by Reich & Beer (1989) and laser Doppler velocimetry by Kikuyama *et al.* (1983*b*), Imao, Itoh & Harada (1996) and Facciolo *et al.* (2007). It should be indicated that in these experiments, typically the pipe rotated while the flow measurement sensors were kept still (relative to the inertial coordinate system fixed to the ground). This treatment method for the system rotation does not explicitly show the Coriolis effects, and is different from the approach based on a rotating coordinate frame (an non-inertial coordinate system), in which Coriolis force appears explicitly in the momentum equation. The latter method of having a Coriolis force term in the momentum equation is often used in the areas of studies such as turbomachinery or meteorology. To be clear, the observations based on the absolute and rotating frames (or inertial and non-inertial frames, respectively) are equivalent, as both reflect the same physical process. For the two velocity fields  $\mathbf{c}$  and  $\mathbf{u}$  observed with respect to the inertial and non-inertial coordinate systems, respectively, they are related by  $\mathbf{c} = \mathbf{u} + \boldsymbol{\Omega} \times \mathbf{r}$ , where  $\boldsymbol{\Omega}$  is the angular speed vector of system rotation and  $\mathbf{r}$  is the position vector relative to the central axis of rotation.

In addition to the experimental approaches, axially rotating pipe flow has also been investigated numerically using Reynolds-averaged Navier–Stokes (RANS) approaches

(Hirai, Takagi & Matsumoto 1988; Speziale, Younis & Berger 2000; Jakirlić, Hanjalić & Tropea 2002), and using LES (Feiz, Ould-Rouis & Lauriat 2003). In these RANS studies, the focus was on the test of turbulence models and analysis of the first- and second-order statistical moments of the velocity field. For example, in the study of Speziale *et al.* (2000), both linear and nonlinear explicit algebraic stress models and second-order closure models were investigated in terms of their predictive performances in the context of an axially rotating flow. In the LES study of Feiz *et al.* (2003), a relatively short pipe length of  $L_z = 20R$  was used for testing axially rotating pipe flows at low rotation numbers of  $Ro_b = 0-4$ , and the obtained LES data were used for studying secondary turbulence structures based on the contours of the instantaneous axial velocity fluctuations and axial vorticity field. Here,  $Ro_b = 2\Omega_z R/U_b$ ,  $U_b$  is the bulk mean velocity defined as  $U_b = \int_0^{2\pi} \int_0^R \langle u_z \rangle r dr d\beta / (\pi R^2)$ , and  $R$  is the radius of the pipe. In the literature on rotating plane-channel and pipe flows (see, e.g., Kristoffersen & Andersson 1993; Grundestam *et al.* 2008; Zhang & Wang 2019), it is popular to use the rotation number to quantify the non-dimensional angular speed of system rotation. However, in the literature on rotating isotropic turbulence, it is popular to use Rossby number, which is simply an inverse of the rotation number and can be defined as  $1/Ro_b$ . Oberlack (1999) studied alternative scaling laws of the mean velocity of an axially rotating pipe flow based on a Lie group theory (also referred to as ‘symmetry analysis’) in contrast to the classical wall-friction-based scaling laws. Their scaling law resulted from symmetry analysis has been validated using the DNS data of Orlandi & Fatica (1997) in the context of axially rotating pipe flows.

In their pioneering DNS studies of axially rotating pipe flows, Orlandi & Fatica (1997), Orlandi (1997) and Ebstein (1998) observed large-scale secondary vortical structures in the pipe centre, which became increasingly elongated as the rotation number increased. The bulk Reynolds number was maintained constant at  $Re_b = 2U_b R/\nu = 4900$  and rotation number ranged from  $Ro_b = 0$  to 20 in these earlier DNS studies. Here,  $\nu$  is the kinematic viscosity of the fluid. Orlandi (1997) performed DNS to compare axially rotating and non-rotating pipe flows, and observed a correlation between the helicity density and the turbulent kinetic energy (TKE) dissipation rate. In the PhD thesis of Ebstein (1998), the statistical moments of the velocity field and budget balances of Reynolds stresses were systematically examined. In their follow-up study, Orlandi & Ebstein (2000) examined the impact of axial system rotation on the budget balances of TKE, Reynolds stresses and enstrophy of the turbulent pipe flow using DNS.

### 1.3. Objectives

Based on a thorough literature review, we note that detailed DNS studies of the axially rotating circular pipe flow are still very limited, and an in-depth understanding of the Coriolis force effects on the flow physics and coherent structures needs to be developed. In view of this, we aim to conduct a systematic DNS study of turbulent pipe flows subjected to axial system rotation for a wide range of rotation numbers.

For a steady-state fully developed axially rotating pipe flow, it is driven by a mean axial pressure gradient and Coriolis forces. Thus, it is anticipated that the energetic flow structures include near-wall streaks and hairpins that are characteristics of a shear-driven boundary layer (whether the flow is subjected to a system rotation or not), and Taylor columns (appearing at moderate and high rotation numbers, as widely observed in rotating isotropic turbulence). It is understood that if the pipe length used in DNS is not long enough to capture the characteristic length scales of energy-containing eddies (such as streaks and Taylor columns), the velocity spectra of the turbulence field at

low wavenumbers would be either artificially distorted or bluntly chopped off. Among the a few DNS studies available in the literature, the longest pipe was that used in Ebstein (1998) and Orlandi & Ebstein (2000), who tested pipe lengths of  $L_z = 15R-25R$  (or  $L_z = 4.775\pi R-7.958\pi R$ ) for axially rotating flows of a fixed Reynolds number of  $Re_b = 4900$  and varying rotation numbers of  $Ro_b = 0-20$ . Owing to the use of small pipe lengths in the DNS studies of axially rotating pipe flows in the current literature, the actual effects of axial system rotation on the characteristic axial length scale of energetic eddies is still unknown. In view of this, as our first research objective, we aim to study flow physics based on precise statistical moments and coherent structures obtained in DNS for a wide range of rotation numbers varying from  $Ro_b = 0$  to 20 at a fixed Reynolds number of  $Re_\tau = 180$  using much longer pipes than those in the literature. Here,  $Re_\tau = u_\tau R/\nu$  is the friction Reynolds number and  $u_\tau$  denotes the wall friction velocity. In order to capture Taylor columns at high rotation numbers, eight DNS cases of very long pipes are considered, which have pipe lengths of  $L_z = 30\pi R-180\pi R$  as the rotation number is increased from  $Ro_b = 0$  to 20.

To precisely demonstrate the impact of pipe lengths on the accuracy of DNS results, DNS-based short pipe lengths needs to be conducted. It is anticipated that use of overly short pipes to perform DNS can lead to spurious results of the statistical moments and spectra of a velocity field. To prove the concept, a complementary comparative study of the pipe length effects on the accuracy of DNS results is conducted, which encompasses eight additional DNS cases of short pipe lengths at two rotation numbers  $Ro_b = 2$  and 20. The short pipe lengths tested vary from  $L_z = \pi R$  to  $7.958\pi R$  for  $Ro_b = 2$  and from  $L_z = \pi R$  to  $80\pi R$  for  $Ro_b = 20$ . The DNS results obtained based on eight short pipes are compared with the accurate results of the longest pipes to determine the minimum pipe length that is required for performing physically accurate DNS of an axially rotating pipe flow, and this constitutes the second objective of this research.

The remainder of this paper is organised as follows. In § 2, the test cases and numerical algorithm are described. In § 3, the axial rotating impacts on the circular pipe flow are analysed by examining the instantaneous and mean flow fields, Reynolds stresses, two-point autocorrelation coefficients, premultiplied spectra of velocity fluctuations, skewness and flatness factors, quadrant analysis of Reynolds stresses and coherent flow structures. In § 4, major findings and conclusions of this research are summarised. Finally, in Appendix A, the complementary comparative study of the pipe length effects on the accuracy of DNS results is reported.

## 2. Test cases and numerical algorithm

Figure 1(a) illustrates schematically a circular pipe under axial system rotation at a constant clockwise angular speed  $\Omega_z$  (about the  $z$ -direction). The radial, azimuthal and axial coordinates of the cylindrical coordinate system are denoted using  $r$ ,  $\beta$  and  $z$ , and the corresponding velocity components are  $u_r$ ,  $u_\beta$  and  $u_z$ , respectively. In order to study the axially rotating effect, a wide range of rotation numbers varying from  $Ro_b = 0$  (non-rotating case) to 20 are compared at a fixed Reynolds number of  $Re_\tau = 180$ . The pipe flow is fully developed such that a periodic boundary condition is applied to the axial direction. No-slip condition is imposed on the pipe surface.

Since the pioneering work of Jiménez & Moin (1991) on the ‘minimum domain’ for DNS of a plane-channel flow, it has become well known that the results of DNS of a wall-bounded flow can be physically incorrect if the computational domain is smaller than the characteristic length scale of the most energetic eddies. Turbulence contains



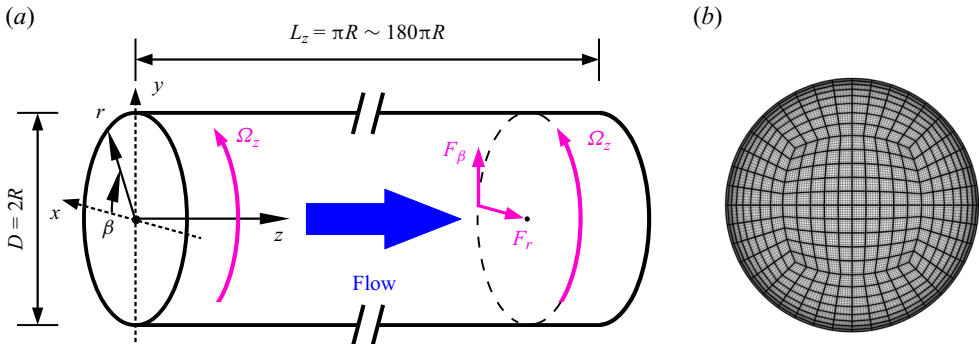


Figure 1. Schematic of turbulent pipe flow subjected to axial system rotation in a cylindrical coordinate system: (a) computational domain and coordinates; (b) mesh in cross-sectional directions. The radial and azimuthal Coriolis force components are  $F_r$  and  $F_\beta$ , respectively. The cross-sectional mesh of the pipe consists of 420 quadrilateral-structural elements based on a spectral-element method. Each element is refined using an eighth-order Gauss–Lobatto–Legendre Lagrange polynomial.

a cascade of wavelengths. If the domain is smaller than the wavelengths of the most energetic eddies, physical phenomena related to those most energetic eddy motions would be missing in DNS, and consequently, a DNS does not reflect the physical reality (even if it is carried out numerically with high-order discretisation schemes and with good convergence). For a steady-state and axially fully developed turbulent pipe flow, the statistical moments (denoted using  $\phi_u$ ) of the turbulent velocity field should be statistically stationary, independent of time  $t$ , axial location  $z$  and pipe length  $L_z$ . Otherwise, if  $\phi_u$  depends on the pipe length (i.e.  $\phi_u = f(L_z)$ ), the DNS results are spurious and unphysical, because the axially fully developed flow condition is violated, which demands  $\partial\phi_u/\partial z \equiv 0$  and  $\partial\phi_u/\partial L_z \equiv 0$ . The goal here is to run high-fidelity DNS that is physically realistic and mathematically accurate, such that the statistical moments of the velocity field are independent of axial pipe length  $L_z$ . Because the flow structures (streaks and Taylor columns) in an axially rotating pipe become increasingly elongated as the rotation number  $Ro_b$  increases, the pipe length  $L_z$  needs to be increased accordingly.

This study includes 16 DNS tests cases listed in [table 1](#) and [table 2](#) of [Appendix A](#), in conformity with the two research objectives aforementioned in § 1.3. For the eight rotation numbers tested, the statistical moments obtained from DNS runs based on the longest pipes are all independent of  $L_z$ . The flow parameters of these eight longest-pipe cases (for the eight rotation numbers tested) are summarised in [table 1](#). Depending upon the rotation number, the pipe length varies from  $L_z = 30\pi R$  to  $180\pi R$ . The choice of these pipe lengths is to ensure that energetic turbulent eddy motions (dominated by streaks at low rotation numbers, and Taylor columns at moderate and high rotation numbers) are reasonably captured in the axial direction at each rotation number. To achieve this goal, even the shortest pipe length of  $L_z = 30\pi R$  is much longer than those used in the current literature, that is,  $L_z = 25R$  or  $7.958\pi R$  in [Ebstein \(1998\)](#) and [Orlandi & Ebstein \(2000\)](#). In addition to the eight longer pipe flow cases summarised in [table 1](#), a complementary comparative study of the pipe length effects on the predictive accuracy of DNS is also conducted in [Appendix A](#), which includes 8 additional DNS cases of short pipes, that is, cases 3A–3C at  $Ro_b = 2$  and 8A–8E at  $Ro_b = 20$ , as summarised in [table 2](#). Through this complementary comparative study, it is proven that statistical moments obtained from DNS runs based on short pipes can be sensitive to  $L_z$ , artificially violating the axially fully developed flow assumption.

Case #	1	2	3	4	5	6	7	8
$Ro_b$	0	1	2	4	6	10	14	20
$Ro_b^A$	0	0.92	1.83	3.67	5.53	9.82	14.77	22.97
$Ro_\tau^A$	0	14.73	29.45	58.88	88.36	147.23	206.09	294.55
$Re_b^A$	5262	5746	5805	5773	5749	5397	5022	4614
$Re_\tau^A$	179.96	179.94	179.97	180.03	179.95	179.99	180.02	179.94
$L_z$	$30\pi R$	$30\pi R$	$30\pi R$	$60\pi R$	$60\pi R$	$90\pi R$	$120\pi R$	$180\pi R$
$N_z$	3600	3600	3600	5400	5400	6000	6400	7200
$N_{tot}$	97 347 600	97 347 600	97 347 600	146 021 400	146 021 400	162 246 000	173 062 400	194 695 200
$\Delta z^+$	4.712	4.712	4.712	6.283	6.283	8.482	10.603	14.137
$(\Delta r^+)_{max}$					3.595			
$(\Delta r^+)_{min}$					0.123			
$(r\Delta\beta^+)_{max}$					5.133			
$(r\Delta\beta^+)_{min}$					0.813			
$(\Delta/\eta)_{max}$	1.92	1.952	1.904	2.044	2.028	2.277	2.492	2.740

Table 1. Summary of eight test cases of the longest pipe at each rotation number.

The governing equations for an incompressible flow with respect to an axially rotating reference frame are

$$\nabla \cdot \mathbf{u} = 0, \tag{2.1}$$

$$\frac{\partial \mathbf{u}}{\partial t} + \mathbf{u} \cdot \nabla \mathbf{u} = -\Pi \hat{e}_z - \frac{1}{\rho} \nabla p + \nu \nabla^2 \mathbf{u} + \mathbf{F}, \tag{2.2}$$

where  $\mathbf{u}$  is the velocity,  $\rho$  is the density of the fluid and  $p = p_s - \rho \Omega_z^2 r^2 / 2$  represents the effective pressure that has absorbed both static pressure  $p_s$  and the centrifugal force. Here  $\Pi$  represents the constant mean axial pressure gradient and  $\hat{e}_z$  is the base unit vector of the  $z$ -direction, with  $|\hat{e}_z| \equiv 1$ . In response to the axial rotation, two components of the Coriolis force ( $\mathbf{F}$ ) appear in the radial and azimuthal directions, i.e.  $F_r = 2\Omega_z u_\beta$  and  $F_\beta = -2\Omega_z u_r$ . Clearly, the instantaneous Coriolis force ( $F_r$  and  $F_\beta$ , defined based on the instantaneous velocities) impacts directly on the velocity field itself ( $u_r$  and  $u_\beta$ , respectively) in a nonlinear manner through (2.2).

The simulations were performed with a spectral-element code ‘Semtex’ made available by Blackburn & Sherwin (2004), which is highly accurate in algorithm suitable for conducting DNS. The computer code was developed using C++ and FORTRAN programming languages, and parallelised following the message passing interface (MPI) standard. As shown in figure 1(b), a quadrilateral-element method was used to divide the cross-section of the pipe into 420 finite elements with each element further discretised spatially using an 8th-order Gauss–Lobatto–Legendre Lagrange (GLLL) polynomial. Time integration is conducted through a three-step second-order time-splitting method developed by Karniadakis, Israeli & Orszag (1991). More specifically, the convection and body force terms (including the mean pressure gradient and Coriolis force) are integrated in the first time substep to result in an intermediate velocity using a second-order backward time-differencing scheme. Subsequently, the intermediate velocity is used in the second time substep to determine the pressure field in order to satisfy the continuity equation. In the last time substep, the viscous term of the momentum equation is implicitly integrated with the prescribed boundary conditions. The last two time substeps rely on solving the 2-D Helmholtz equations in the spectral space based on a static condensation technique introduced by Karniadakis & Sherwin (2005). So far, this code has been used by our group

$Ro_b$	2	2	2	2	20	20	20	20	20	20	20	20	20
Case #	3A	3B	3C	3	8A	8B	8C	8D	8E	8	8	8	8
$Ro_b^A$	1.84	1.86	1.83	1.83	16.86	17.96	19.4	21.9	23	22.97	22.97	22.97	22.97
$Ro_t^A$	29.32	29.41	29.47	29.45	293.91	294.39	294.39	295.11	294.50	294.55	294.55	294.55	294.55
$Re_b^A$	5770	5684	5799	5805	6287	5902	5463	4840	4608	4614	4614	4614	4614
$Re_t^A$	180.74	180.2	179.87	179.97	180.33	180.03	180.03	179.6	179.96	179.94	179.94	179.94	179.94
$L_z$	$\pi R$	$2\pi R$	$7.958\pi R$	$30\pi R$	$\pi R$	$2\pi R$	$7.958\pi R$	$30\pi R$	$80\pi R$	$180\pi R$	$180\pi R$	$180\pi R$	$180\pi R$
$N_z$	120	240	960	3600	120	240	960	3600	4800	7200	7200	7200	7200
$N_{tot}$	3244920	6489840	25959360	97347600	3244920	6489840	25959360	97347600	129796800	194695200	194695200	194695200	194695200
$\Delta z^+$	4.712	4.712	4.688	4.712	4.712	4.712	4.688	4.712	9.425	14.137	14.137	14.137	14.137
$(\Delta r^+)_{max}$						3.595							
$(\Delta r^+)_{min}$						0.123							
$(r\Delta\beta^+)_{max}$						5.133							
$(r\Delta\beta^+)_{min}$						0.813							
$(\Delta/\eta)_{max}$	1.979	1.945	1.917	1.904	2.025	1.977	1.92	1.895	2.4	2.740	2.740	2.740	2.740

Table 2. Test cases for the comparative study of the pipe length effects at  $Ro_b = 2$  and 20.



## DNS of turbulent pipe flow subjected to axial rotation

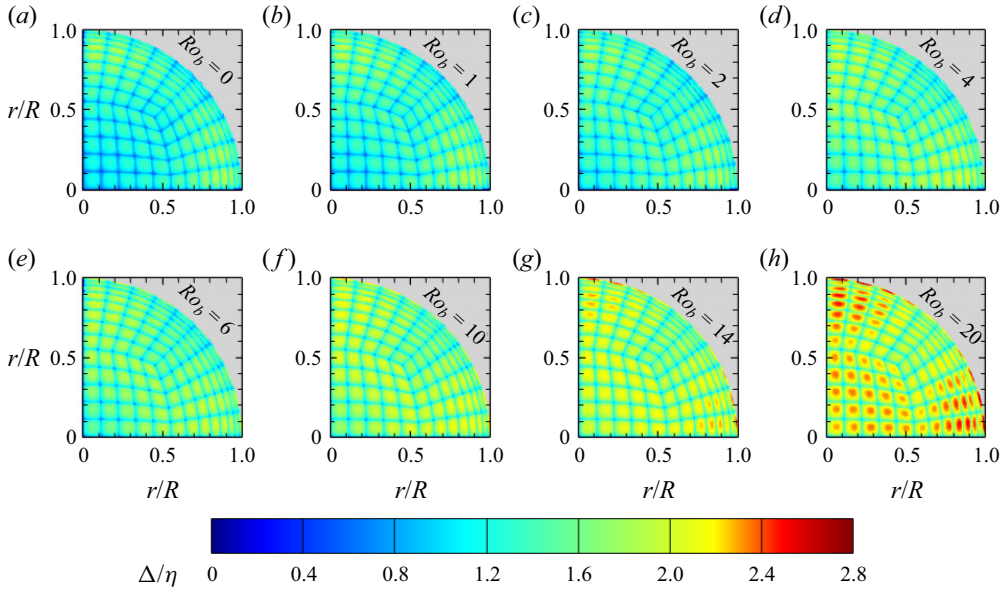


Figure 2. Contours of the ratio of the grid size to the Kolmogorov length scale  $\Delta/\eta$ . Given the axial symmetry of the flow field, only a quarter cross-section of the pipe is plotted for each rotation number  $Ro_b = 0$ –20. Results are based on test cases of the longest pipes at corresponding rotation numbers listed in [table 1](#).

for conducting DNS studies of spanwise-rotating turbulent square duct flows and heat transfer (Fang *et al.* 2017; Fang & Wang 2018), spanwise-rotating turbulent elliptical pipe flows and heat transfer (Rosas, Zhang & Wang 2021; Rosas & Wang 2022), and radially rotating turbulent circular pipe flows (Zhang & Wang 2019).

The pipe lengths and grid resolutions of the eight test cases of the longest pipes are shown in [table 1](#). All physical quantities are expanded into the spectral space using Fourier series with 3600–7200 modes ( $N_z$ ) in the  $z$ -direction for pipes of different lengths. As indicated by [table 1](#), the total number of nodes varies from  $N_{tot} = 97.3$  to 194.7 million for the 8 test cases. The calculation of  $N_{tot}$  is directly based on the number of Fourier modes in the axial direction and the number of the eighth-order GLLL orthogonal polynomial interpolants (within each of the 420 finite elements) in the cross-stream directions. Both Fourier series and the GLLL orthogonal polynomial offer very high numerical discretisation accuracies. In each test case, the grid spacing is uniform in the streamwise direction with  $\Delta z^+ = 4.712$ –14.137, and varies in the radial and azimuthal directions with  $\Delta r^+ = 0.123$ –3.595 and  $r\Delta\beta^+ = 0.813$ –5.133. Here, superscript ‘+’ denotes the wall coordinate calculated through non-dimensionalisation based on the kinematic viscosity of the fluid  $\nu$  and wall friction velocity  $u_\tau$  (defined as  $u_\tau = \sqrt{-\tau R/2}$ ). To satisfy the demanding requirement of DNS on grid resolution for capturing the smallest scale of turbulence, the grid size needs to be kept at the same order as the Kolmogorov length scale, i.e.  $O(\Delta/\eta) \sim O(1)$ . [Figure 2](#) shows the ratio  $\Delta/\eta$  for the eight test cases of the longest pipes listed in [table 1](#). The grid size is defined as  $\Delta = [(\Delta r) \times (r\Delta\beta) \times (\Delta z)]^{1/3}$  and the Kolmogorov length scale is determined by  $\eta = (\nu^3/\varepsilon)^{1/4}$ , where  $\varepsilon$  is the dissipation rate of TKE. From the figure, it is clear that the strict grid resolution requirement of  $\Delta/\eta = O(1)$  for accurately performing DNS is satisfied. The maximum value of  $\Delta/\eta$  of each of all 16 test cases is given in [tables 1](#) and [2](#), which varies from 1.904 to 2.740.

The axial system rotation has a direct impact on the bulk mean velocity  $U_b$  such that the actual calculated rotation number  $Ro_b^A$  deviates considerably from its nominal value

$Ro_b$  (see table 1). Here, superscript ‘A’ denotes the actual result calculated using the DNS data. By contrast, the value of the wall friction velocity  $u_\tau$  is insensitive to the axial system rotation. Consequently, the wall-friction-velocity-based rotation number  $Ro_\tau = 2\Omega_z R/u_\tau$  varies linearly with the angular speed  $\Omega_z$  and the value of the wall-friction-velocity-based Reynolds number  $Re_\tau^A$  varies little from its nominal value of  $Re_\tau = 180$ . The values of rotation numbers  $Ro_b$ ,  $Ro_b^A$  and  $Ro_\tau^A$ , and Reynolds numbers  $Re_b^A$  and  $Re_\tau^A$  of the 16 test cases associated with the two research objectives are given in tables 1 and 2.

We started simulations with a laminar solution added with arbitrary perturbations, and statistics were collected after the pipe flow became statistically stationary. All DNS calculations were conducted on the Alliance (Digital Research Alliance of Canada) supercomputers. For the 8 test cases of the longest pipes listed in table 1, 300 instantaneous snapshots of the flow field over 40 large-eddy turnover times (LETOTs, defined as  $R/u_\tau$ ) were collected for cases 1–7, whereas 600 instantaneous snapshots were collected over 80 LETOTs for case 8. For each simulated case, approximately 1.4–4.5 TB data are stored on the server. However, for the cases of short pipe lengths (of  $L_z = \pi R - 7.958\pi R$ ) listed in table 2, 900–1200 instantaneous snapshots of the flow fields over 122–163 LETOTs were collected for computing the flow statistics.

In our analysis, an instantaneous turbulence variable  $\phi$  is decomposed as  $\phi = \langle \phi \rangle + \phi'$ , where  $\langle \phi \rangle$  is the temporally and spatially averaged component over the homogeneous ( $\beta$  and  $z$ ) directions, and  $\phi'$  represents the residual fluctuating component. To make it convenient for studying the wall-scaling behaviour of the flow in a circular pipe in analogous to a turbulent boundary-layer flow over a flat plate, a dimensionless coordinate measured from the wall can be introduced, i.e.  $y \stackrel{\text{def}}{=} 1 - r/R$ , and the corresponding wall coordinate can be defined as  $y^+ \stackrel{\text{def}}{=} (R - r)u_\tau/\nu$  (or,  $y^+ \stackrel{\text{def}}{=} yRe_\tau$ ).

### 3. Results and discussion

This result analysis includes two parts to examine: (i) the impact of axial system rotation on the velocity field of the pipe flow based on a comparative study of eight rotation numbers of  $Ro_b = 0-20$  (with the longest pipe at each rotation number) given in table 1; and (ii) the impact of pipe length on the predictive accuracy of DNS based on 10 cases of varying pipe lengths at 2 rotation numbers  $Ro_b = 2$  and 20 given in table 2. Part (ii) represents a complementary study for part (i) by establishing a knowledge foundation to ensure that the DNS results of part (i) are physically accurate obtained using sufficiently long pipes. In this section, the results of part (i) are analysed, whereas those of part (ii) are presented in Appendix A. In the following, the characteristics of the instantaneous flow are first discussed, followed by an analysis of statistical moments of the velocity field, premultiplied energy spectra, high-order turbulence statistics and turbulence structures.

#### 3.1. Instantaneous flow fields

Figure 3 shows contours of the instantaneous axial velocity  $u_z^+$  (left half of each panel) and instantaneous axial vorticity  $\omega_z^+$  (right half of each panel) in the cross-stream plane of flows at different rotation numbers. Here, the axial vorticity is defined as  $\omega_z = [\partial(ru_\beta)/\partial r - \partial u_r/\partial \beta]/r$ . All contours are depicted at the same axial streamwise location of  $z/R = 20\pi$  and the same time instant of  $t = 20.38$  LETOTs. As is clear from the left half of figure 3(a), in a non-rotating pipe, the flow structures show ‘mushroom patterns’ in the near-wall region where several pairs of small counter-rotating vortices

## DNS of turbulent pipe flow subjected to axial rotation

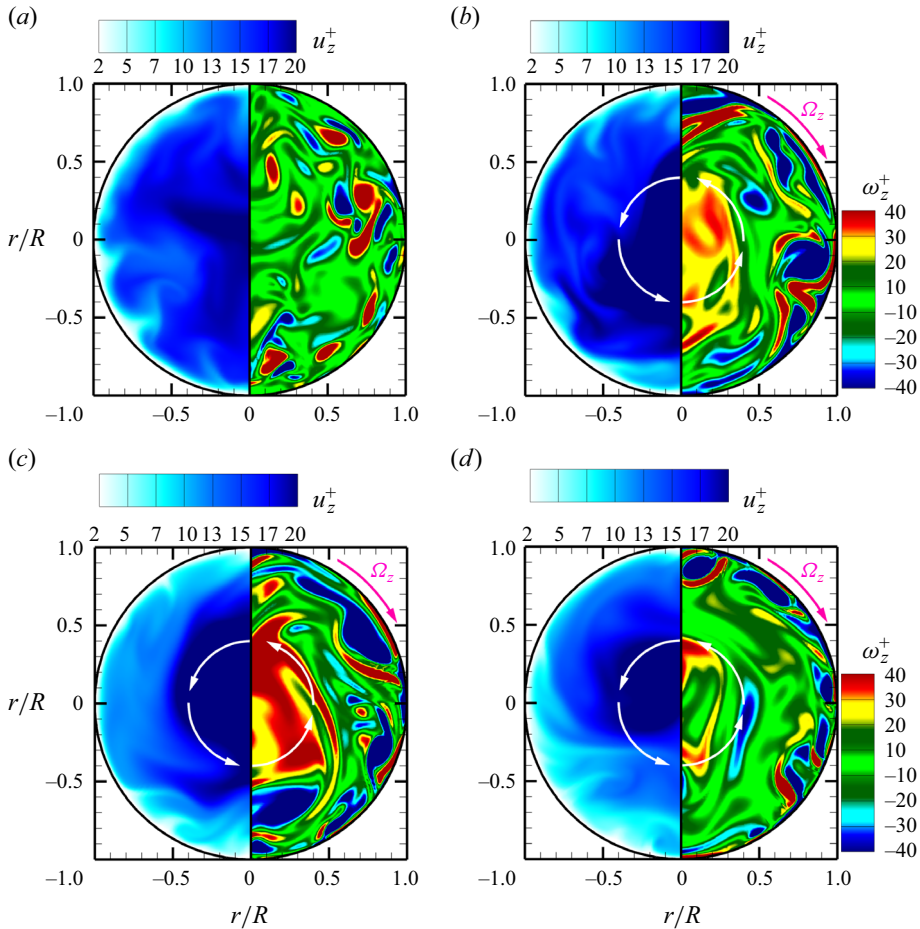


Figure 3. (a)–(d) Cross-stream view of instantaneous axial velocity  $u_z^+$  (left half of each panel) and instantaneous axial vorticity  $\omega_z^+$  (right half of each panel) of the non-rotating ( $Ro_b = 0$ ) and rotating ( $Ro_b = 4, 14$  and  $20$ ) pipe flows, respectively. White arrows indicate the counterclockwise rotating direction of the secondary flow. All contours are plotted at the same axial location (at  $z/R = 20\pi$ ) and the same time instant (at  $t = 20.38$  LETOTs). The values of  $u_z$  and  $\omega_z$  have been non-dimensionalised using  $u_\tau$ . Results are based on test cases of the longest pipes at corresponding rotation numbers listed in table 1.

are observed. From figure 3(b), it is observed that because of the axial system rotation imposed (at  $Ro_b = 4$ ), a large counterclockwise-rotating secondary-flow structure appears at the pipe centre, clearly indicated by the contours of positively valued  $\omega_z^+$  (shown in red). As the rotation number continues to increase to  $Ro_b = 14$  as shown in figure 3(c), the secondary flow structures indicated by the positively valued  $\omega_z^+$  become the most intense, significantly stretched in the azimuthal direction. The counterclockwise-rotating secondary-flow structures observed at relatively high rotation numbers are the so-called Taylor columns, which become increasingly elongated in the axial direction as the rotation number is increased.

### 3.2. Mean flow fields

Figure 4 compares the cross-stream distributions of the mean axial velocity  $\langle u_z \rangle^+$  and TKE ( $k^+ = \langle u_i' u_i' \rangle / 2$ ) of four different rotation numbers. Given the axial symmetry of the flow field, only a quarter of the domain is plotted for each rotation number to facilitate

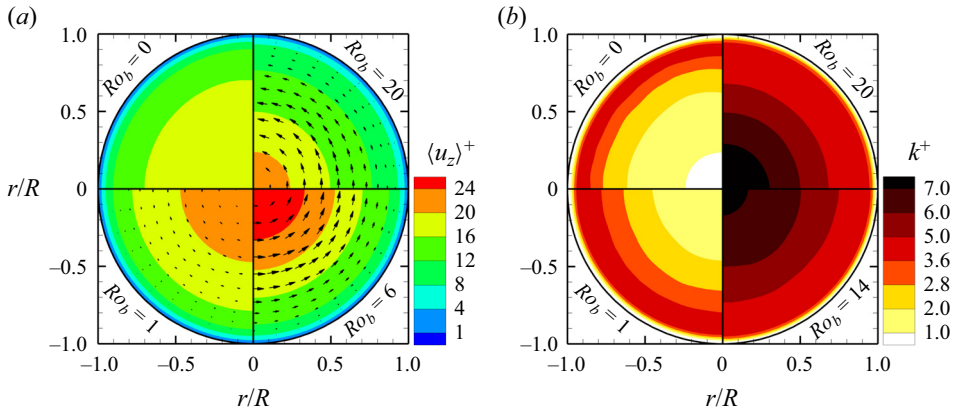


Figure 4. Cross-stream view of (a) mean axial velocity  $\langle u_z \rangle^+$  and (b) TKE  $k^+$  at four different rotation numbers for  $Ro_b = 0-20$ . The direction of the system rotation is clockwise, identical to that shown in figure 3. In panel (a), the contours are superimposed with mean cross-stream velocity vectors indicated by black arrows. The values of  $\langle u_z \rangle^+$  and  $k^+$  have been non-dimensionalised based on  $u_\tau$ . Results are based on test cases of the longest pipes at corresponding rotation numbers listed in table 1.

a direct comparison. In figure 4(a), the contours of  $\langle u_z \rangle^+$  are superimposed with mean cross-stream velocity vectors for  $Ro_b = 0, 1, 6$  and  $20$ . In figure 4(b), the contour plots of  $k^+$  are based on rotation numbers  $Ro_b = 0, 1, 14$  and  $20$ . By comparing the mean flow patterns at  $Ro_b = 0$  and  $1$  shown in figure 4(a), it can be seen that as soon as the system rotation is imposed, mean secondary-flow motion occurs, behaving as counterclockwise rotations as indicated by the mean cross-stream velocity vectors. From figure 4(a), it is observed that in general, the magnitude of  $\langle u_z \rangle^+$  increases monotonically as the pipe centre is approached for both rotating and non-rotating flow cases. The magnitude of  $\langle u_z \rangle^+$  at the pipe centre reaches its maximum at  $Ro_b = 6$ . However, as the rotation number further increases from  $Ro_b = 6$  to  $20$ , the magnitude of  $\langle u_z \rangle^+$  reduces. This non-monotonic trend in the value of  $\langle u_z \rangle^+$  with an increasing rotation number is interesting, and will be studied further by examining the evolution of the bulk mean velocity  $U_b^+$  with  $Ro_b$ . The variation of the TKE distribution in response to an increasing rotation number also exhibits an interesting trend. As shown in figure 4(b), for a non-rotating pipe flow ( $Ro_b = 0$ ), the peak value of  $k^+$  occurs in the buffer layer (at approximately  $y^+ = 15$ ). Clearly, as the value of  $Ro_b$  increases, the magnitude of  $k^+$  increases in general and, furthermore, the radial distribution of the  $k^+$  value varies. More specifically, as the rotation number is increased to  $Ro_b = 14$ , the peak value of  $k^+$  shifts to the pipe centre, a pattern that is in sharp contrast to that of the non-rotating flow ( $Ro_b = 0$ ). As the rotation number continues to increase from  $Ro_b = 14$  to  $20$ , the region of large  $k^+$  values expands slightly at the pipe centre.

Figure 5 compares the profiles of the mean axial velocity  $\langle u_z \rangle^+$ , mean swirl velocity  $r\langle u_\beta \rangle^+/R$  and mean axial vorticity  $\langle \omega_z \rangle^+$  with respect to the non-dimensional wall-normal distance ( $y$ ) of the eight test cases of table 1. Given its axial symmetry, only one half the profile of  $\langle u_z \rangle^+$  is plotted in figure 5(a), which varies from the pipe wall to the pipe centre (for  $y \in [0, 1]$ ). From figure 5(a), it is evident that the magnitude of  $\langle u_z \rangle^+$  varies non-monotonically with an increasing  $Ro_b$  value. At the pipe centre, the peak value of  $\langle u_z \rangle^+$  increases when the rotation number rises from  $Ro_b = 0$  to  $6$ , and reaches its maximum at  $Ro_b = 6$  with a magnitude that is 40.19 % higher than that of the non-rotating pipe flow. As  $Ro_b$  continues to increase from  $6$  to  $20$ , the peak value of  $\langle u_z \rangle^+$  reduces, which however is still larger than that of the non-rotating pipe flow ( $Ro_b = 0$ ). These

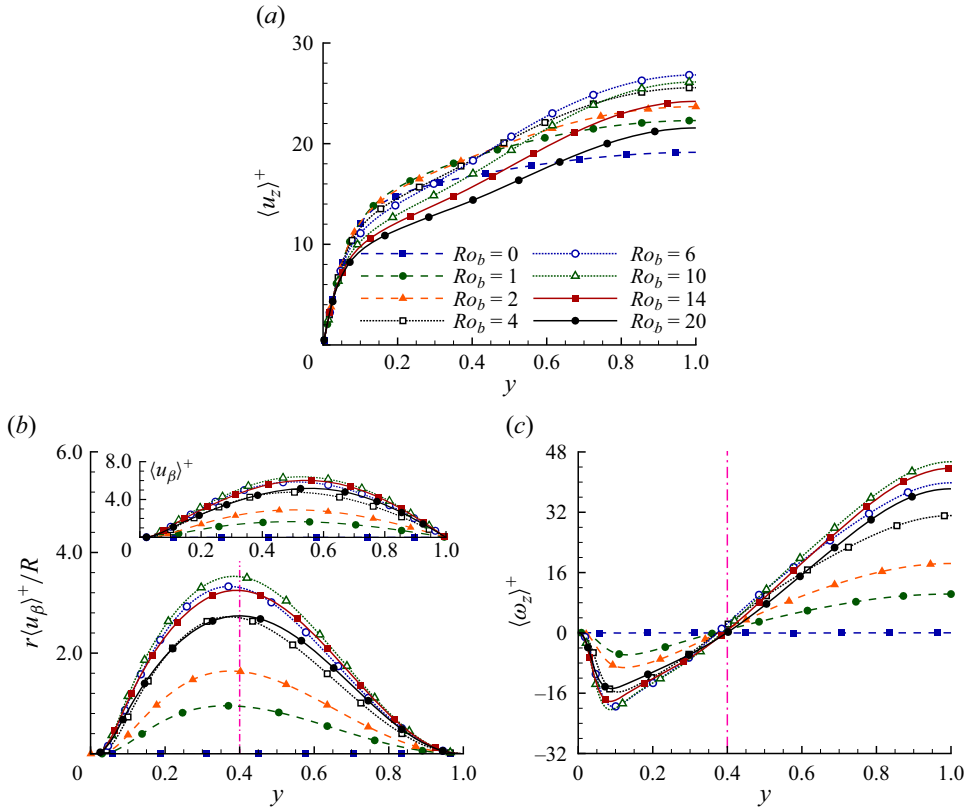


Figure 5. Profiles of (a) mean axial velocity  $\langle u_z \rangle^+$ , (b) mean swirl velocity  $r\langle u_\beta \rangle^+/R$  and (c) mean axial vorticity  $\langle \omega_z \rangle^+$  at eight rotation numbers for  $Ro_b = 0-20$  based on test cases listed in table 1. In panel (b), the profiles of  $\langle u_\beta \rangle^+$  at different rotation numbers are displayed using a subpanel. In panels (b,c), the pink vertical dash-dotted line demarcates the location of zero value of  $\langle \omega_z \rangle^+$  occurring at  $y = 0.4$ . All values have been non-dimensionalised by  $u_\tau$ .

observations are qualitatively consistent with figure 4(a). From the subpanel of figure 5(b), it is clear that the profile of  $\langle u_\beta \rangle^+$  is zero at both the pipe wall and pipe centre. In addition, it is interesting to observe from figure 5(b,c) that both  $r\langle u_\beta \rangle^+/R$  and  $\langle \omega_z \rangle^+$  reach their maxima at  $Ro_b = 10$ , and the peak of  $r\langle u_\beta \rangle^+/R$  is located at  $y \approx 0.4$  where the mean axial vorticity  $\langle \omega_z \rangle^+$  is zero identically.

Figure 6 compares the bulk mean velocity  $U_b^+$  and volume-averaged TKE  $k_m^+$  at varying rotation numbers based on the test cases listed in table 1. In figure 6(a), the profile of  $U_b^+$  peaks at  $Ro_b = 2$  (or generally in the range of  $Ro_b \in [1, 6]$ ), with a magnitude that is 10.33 % higher than that of the non-rotating pipe flow. As the rotation number is increased beyond 6, the magnitude of  $U_b^+$  decreases significantly. At the highest rotation number  $Ro_b = 20$ , the value of  $U_b^+$  is 12.32 % lower than that of the non-rotating flow. The monotonic decreasing trend of  $U_b^+$  with respect to an increasing value of  $Ro_b$  (at high rotation numbers of  $Ro_b \geq 6$ ) is vividly demonstrated in figure 4(a), and is also consistent with the trend of the mean axial velocity profiles of  $\langle u_z \rangle^+$  shown in figure 5(a) and the result of Orlandi & Ebstein (2000). From figure 6(b), the value of  $k_m^+$  increases as the rotation number increases in general, and reaches its maximum at  $Ro_b = 14$ . However, as the rotation number is increased from  $Ro_b = 14$  to 20, the value of  $k_m^+$  varies little.



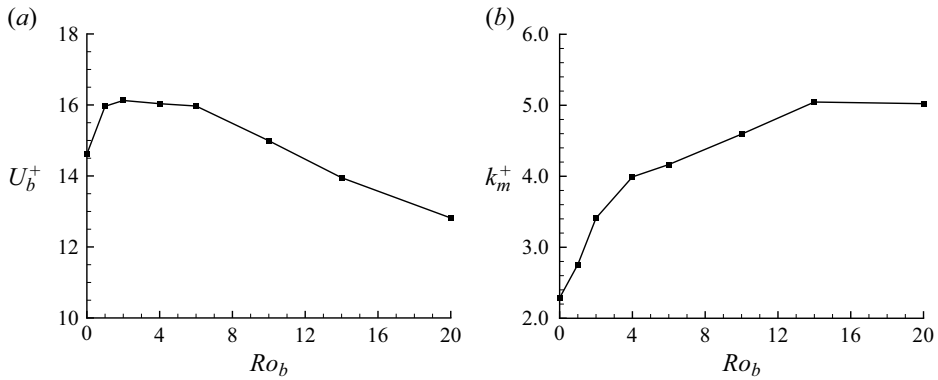


Figure 6. Profiles of (a) bulk mean velocity  $U_b^+$  and (b) volume-averaged TKE  $k_m^+$  with respect to the rotation number  $Ro_b$ . The values of  $U_b^+$  and  $k_m^+$  have been non-dimensionalised based on  $u_\tau$ . Results are based on test cases of the longest pipes at corresponding rotation numbers listed in table 1.

We explain later that axial rotation enhances the magnitudes of  $\langle u'_r u'_r \rangle^+$  and  $\langle u'_\beta u'_\beta \rangle^+$ , which subsequently make a positive contribution to the value of  $k_m^+$ .

### 3.3. Reynolds stresses

Figure 7 compares the profiles of six Reynolds stresses  $\langle u'_z u'_z \rangle^+$ ,  $\langle u'_r u'_r \rangle^+$ ,  $\langle u'_\beta u'_\beta \rangle^+$ ,  $\langle u'_r u'_z \rangle^+$ ,  $\langle u'_r u'_\beta \rangle^+$  and  $\langle u'_\beta u'_z \rangle^+$  at eight rotation numbers of  $Ro_b = 0-20$  based on test cases of table 1. All these Reynolds stress profiles shown are axially symmetrical about the pipe centre (located at  $y = 1.0$ ). As shown in figure 7(a), the profile of  $\langle u'_z u'_z \rangle^+$  peaks at  $y = 0.083$  (or  $y^+ \approx 15$ ) in the near-wall region of the non-rotating pipe flow. As the rotation number is increased, the magnitude of  $\langle u'_z u'_z \rangle^+$  reduces monotonically in the near-wall region of the pipe. Furthermore, the peak of  $\langle u'_z u'_z \rangle^+$  moves towards the pipe centre as  $Ro_b$  increases. The lowest and highest peak values occur at  $Ro_b = 4$  and 14, respectively, which are 15.01 % and 4.57 % lower than that of the non-rotating pipe flow ( $Ro_b = 0$ ). In addition, it is interesting to observe that the magnitude of  $\langle u'_z u'_z \rangle^+$  increases monotonically with an increasing rotation number at the pipe centre. At  $Ro_b = 20$ , the magnitude of  $\langle u'_z u'_z \rangle^+$  increases by more than fivefold in comparison with the non-rotating flow ( $Ro_b = 0$ ). The observations of the apparent migration of the peak of  $\langle u'_z u'_z \rangle^+$  towards the pipe centre at higher rotation numbers (for  $Ro_b \geq 6$ ) and the monotonic increasing trend of the magnitude of  $\langle u'_z u'_z \rangle^+$  with an increasing rotation number at the pipe centre are the result of Taylor columns. The appearance of the Taylor columns at moderate and high rotation numbers also significantly affects the physical features of the mean flow field, e.g. the reduction of the bulk mean velocity  $U_b^+$  with an increasing rotation number shown previously in figure 6(a). The characteristics of these two types of coherent flow structures, hairpins and Taylor columns, are studied in detail in both physical and spectral spaces in §§ 3.4 and 3.6.

As is clear in figure 7(b,c), the magnitudes of  $\langle u'_r u'_r \rangle^+$  and  $\langle u'_\beta u'_\beta \rangle^+$  increase monotonically in the pipe centre as the rotation number is increased. Furthermore, as the rotation number rises, the profile of  $\langle u'_r u'_r \rangle^+$  evolves from a dual-peak pattern to a single-peak pattern (over the entire radial direction along a diameter across the pipe), but that of  $\langle u'_\beta u'_\beta \rangle^+$  turns into a triple-peak pattern over the full range of a diameter.



DNS of turbulent pipe flow subjected to axial rotation

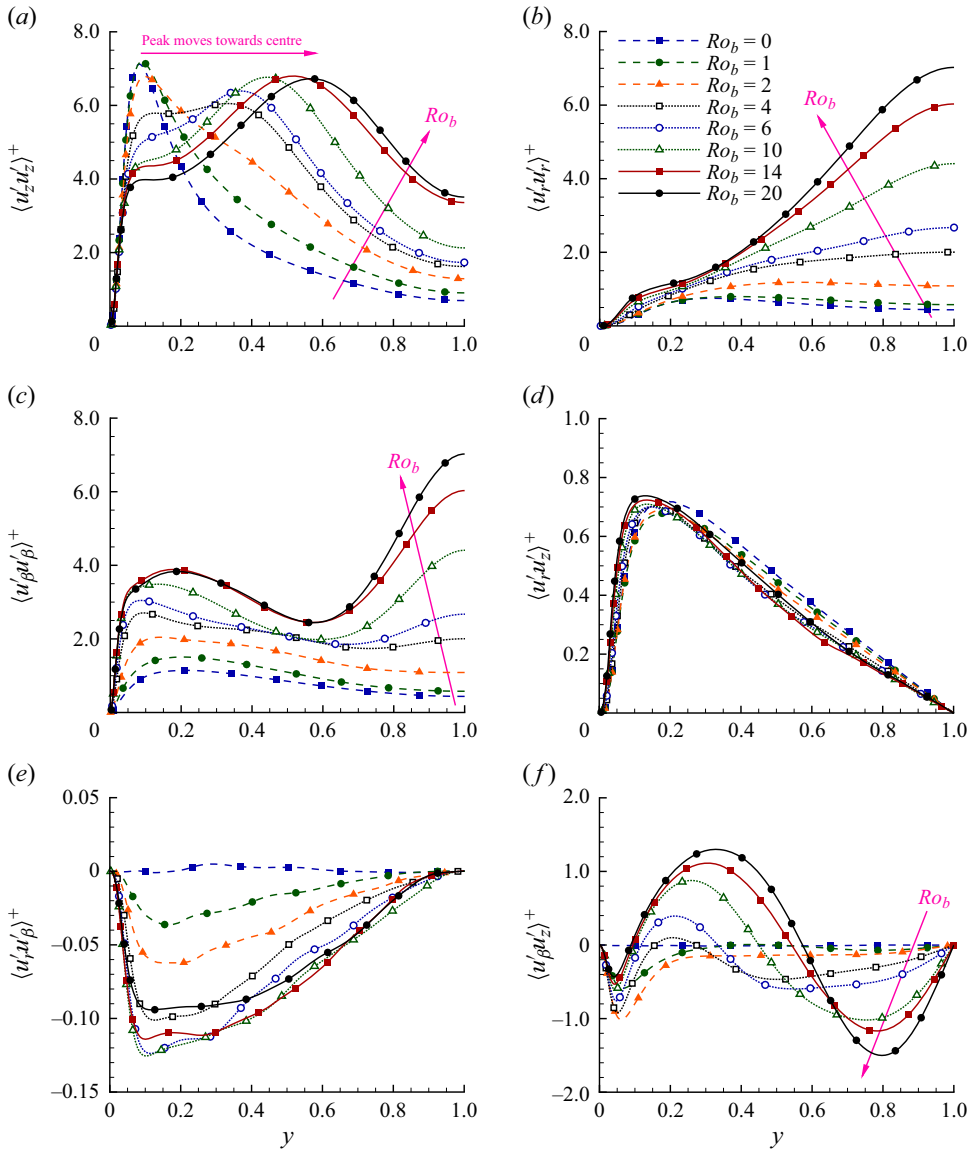


Figure 7. Profiles of six Reynolds stresses (a)  $\langle u'_z u'_z \rangle^+$ , (b)  $\langle u'_r u'_r \rangle^+$ , (c)  $\langle u'_\beta u'_\beta \rangle^+$ , (d)  $\langle u'_r u'_z \rangle^+$ , (e)  $\langle u'_r u'_\beta \rangle^+$  and (f)  $\langle u'_\beta u'_z \rangle^+$  at eight different rotation numbers for  $Ro_b = 0-20$  based on test cases of table 1. Pink arrows point to the direction of an increasing rotating effect. All values are non-dimensionalised by  $u_\tau^2$ .

In response to the system rotation imposed, secondary flows are induced, which tend to enhance the general levels of  $\langle u'_z u'_z \rangle^+$ ,  $\langle u'_r u'_r \rangle^+$  and  $\langle u'_\beta u'_\beta \rangle^+$ , especially in the central region of the pipe. As a result, the level of the volume-averaged TKE  $k_m^+$ , shown previously in figure 6(b), enhances as the rotation number increases within the range of this study (for  $Ro_b \in [0, 20]$ ).

From figure 7(d), it is clear that the profile of  $\langle u'_r u'_z \rangle^+$  is approximately linear and symmetrical in the central region of the circular pipe for both non-rotating and rotating flows. For the non-rotating flow case, the profile of  $\langle u'_r u'_z \rangle^+$  peaks at  $y = 0.177$  (or

$y^+ \approx 32$ ). However, as the rotation number is increased, the peak position of  $\langle u'_r u'_z \rangle^+$  shifts slightly towards the wall, with its profile being relatively insensitive to the rotation number. For a non-rotating flow, it is well-known that  $\langle u'_r u'_\beta \rangle^+ \equiv 0$  and  $\langle u'_\beta u'_z \rangle^+ \equiv 0$  hold strictly due to the axial symmetry of the flow. However, this is not the case for an axially rotating pipe flow. As is evident in figure 7(e,f), both these Reynolds shear stress components are non-trivial in an axially rotating pipe flow, albeit their magnitudes are one order of magnitude smaller than those of the other four Reynolds normal and shear stress components. Furthermore, as shown in figure 7(e), an approximately linear behaviour can be observed in the profile of  $\langle u'_r u'_\beta \rangle^+$  as soon as the axial system rotation is imposed (for  $Ro_b \geq 1$ ), which is a consequence of clockwise system rotation of the pipe. This observation is consistent with the finding by Orlandi & Fatica (1997). Figure 7(f) shows the radial profile of  $\langle u'_\beta u'_z \rangle^+$ . Clearly, the value of  $\langle u'_\beta u'_z \rangle^+$  is zero identically at the pipe wall ( $y = 0$ ) and at the pipe centre ( $y = 1.0$ ), due to the no-slip and axial-symmetry flow conditions, respectively. As the rotation number is increased, the amplitude of  $\langle u'_\beta u'_z \rangle^+$  increases monotonically. At high rotation numbers of  $Ro_b \geq 14$ , it is interesting to observe that the value of  $\langle u'_\beta u'_z \rangle^+$  changes sign three times within half a radial domain (for  $y \in [0, 1]$ ), such that there are five zero-crossing points along the entire radial direction of a diameter.

The behaviours of the three components of Reynolds shear stresses associated with figure 7(d-f) can be further analysed through their corresponding shear stress balance equations. Assuming that the flow is fully developed in the axial direction, and statistically homogeneous in the axial and azimuthal directions, the following equations can be obtained from the  $z$ -,  $\beta$ - and  $r$ -components of the momentum equation (2.2) after applying turbulence decomposition (i.e.  $u_i = \langle u_i \rangle + u'_i$ ) to the velocity (Speziale *et al.* 2000)

$$\frac{\nu}{r} \frac{d}{dr} \left( r \frac{d\langle u_z \rangle}{dr} \right) - \frac{1}{r} \frac{d}{dr} \left( r \langle u'_r u'_z \rangle \right) = \Pi, \tag{3.1}$$

$$\nu \frac{d}{dr} \left[ \frac{1}{r} \frac{d}{dr} \left( r \langle u_\beta \rangle \right) \right] - \frac{1}{r} \frac{d}{dr} \left( r \langle u'_r u'_\beta \rangle \right) - \frac{\langle u'_r u'_\beta \rangle}{r} = 0, \tag{3.2}$$

$$\langle u'_\beta u'_\beta \rangle - \langle u'_r u'_r \rangle = -\langle u_\beta \rangle \langle u_\beta \rangle + r \left( \frac{1}{\rho} \frac{d\langle p \rangle}{dr} + \frac{d\langle u'_r u'_r \rangle}{dr} - 2\Omega_z \langle u_\beta \rangle \right). \tag{3.3}$$

Note that in the derivation of (3.2) from the  $\beta$ -component of the momentum equation, the mean azimuthal Coriolis force  $\langle F_\beta \rangle$  is zero identically because  $\langle u_r \rangle \equiv 0$ . Both viscous shear and Reynolds shear stresses vanish from (3.3), the simplified  $r$ -component of the momentum equation. From (3.3), it is clear that at pipe centre (where  $r = 0$  or  $y = 1.0$ ),  $\langle u'_\beta u'_\beta \rangle - \langle u'_r u'_r \rangle = 0$ . This explains the observation in figure 7(b,c) that the trends and magnitudes of  $\langle u'_\beta u'_\beta \rangle$  and  $\langle u'_r u'_r \rangle$  become increasingly similar as the pipe centre is approached. In a fully developed pipe flow,  $\tau_{\beta z}^{vis} = \tau_{z\beta}^{vis} \equiv 0$ . In (3.1) and (3.2), the remaining two non-trivial mean viscous shear stresses are defined as (Reich & Beer 1989)

$$\tau_{rz}^{vis} = \nu \frac{\partial \langle u_z \rangle}{\partial r} \quad \text{and} \quad \tau_{r\beta}^{vis} = \nu r \frac{\partial}{\partial r} \left( \frac{\langle u_\beta \rangle}{r} \right), \tag{3.4a,b}$$

respectively. The total shear stresses balance as

$$\tau_{ri}^{tot} = \tau_{ri}^{vis} - \langle u'_r u'_i \rangle, \tag{3.5}$$

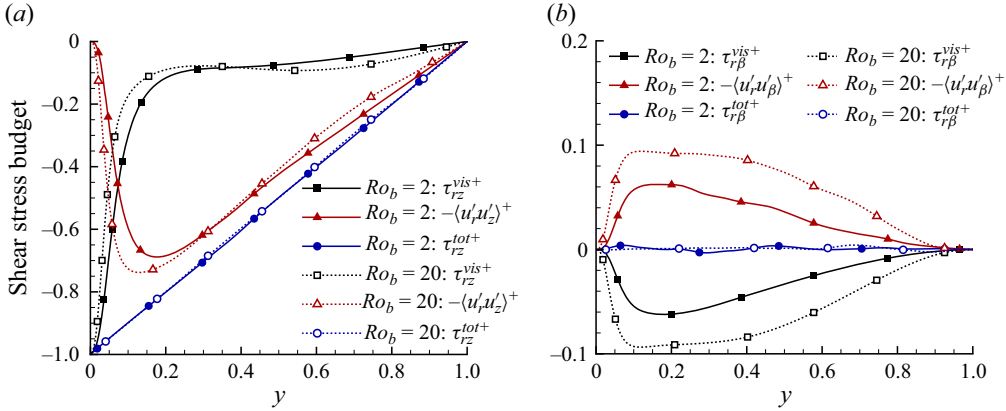


Figure 8. Budget profiles of mean shear stress  $\tau_{rz}^+$  and  $\tau_{r\beta}^+$  at two rotation numbers  $Ro_b = 2$  and 20 based on test cases of the longest pipes of table 1. All shear stress budget terms are non-dimensionalised by  $u_\tau^2$ . Panel (a) shows radial-axial shear stress components ( $\tau_{rz}^{vis+}$  and  $-\langle u'_r u'_z \rangle^+$ ). Panel (b) shows radial-azimuthal shear stress components ( $\tau_{r\beta}^{vis+}$  and  $-\langle u'_r u'_\beta \rangle^+$ ).

where  $i$  denotes  $z$  or  $\beta$ . The budget balance of total shear stresses in non-dimensional forms (i.e.  $\tau_{rz}^{tot+}$  and  $\tau_{r\beta}^{tot+}$ ) is displayed in figure 8. The linear behaviour of  $\tau_{rz}^{tot+}$  is evident from (3.1), whose non-dimensional form may be expressed as

$$\tau_{rz}^{tot+} = \tau_{rz}^{vis+} - \langle u'_r u'_z \rangle^+ = y - 1, \quad (3.6)$$

in the context of an axially rotating pipe flow. From figure 8(a), the profile of  $-\langle u'_r u'_z \rangle^+$  changes slightly in its shape as the rotation number is increased from  $Ro_b = 2$  to 20. The reason the profile of  $-\langle u'_r u'_z \rangle^+$  is insensitive to  $Ro_b$  is that its value is linearly related to the viscous shear stress such that the total shear stress varies as  $\tau_{rz}^{tot+} = y - 1$  for both rotating and non-rotating pipe flows. From (3.6), it is understood that at the wall ( $y = 0$ )  $\langle u'_r u'_z \rangle^+|_w \equiv 0$ , and so the non-dimensional wall-shear stress becomes  $\tau_w^+ = \tau_{rz}^{vis+}|_w \equiv -1$ . Therefore, for axially rotating pipe flows of different rotation numbers, the wall shear stress  $\tau_w$  is expected to be constant, which is evidenced by the stable values of the calculated wall friction number  $Re_\tau^A$  listed in table 1. Furthermore, because the wall shear stress  $\tau_w$  is constant, it is inferred that the skin friction coefficient, defined as  $C_f = \tau_w / (\rho U_b^2 / 2)$ , is proportional to  $U_b^{-2}$  with the value of  $U_b$  given in figure 6(a).

From figure 8(b), it is interesting to observe that the profile of  $\tau_{r\beta}^{vis+}$  is almost a mirror reflection of that of Reynolds stress  $-\langle u'_r u'_\beta \rangle^+$  such that the total shear stress is zero, i.e.  $\tau_{r\beta}^{tot+} = 0$ . This is an expected feature, which can be strictly proven as follows. Equation (3.2) is derived from the  $\beta$ -component of the momentum equation, which can also be written as  $\nabla \cdot \tau_{r\beta}^{tot} = 0$ , or

$$\frac{\partial \tau_{r\beta}^{tot}}{\partial r} + \frac{2\tau_{r\beta}^{tot}}{r} = 0. \quad (3.7)$$

The solution to the above equation is

$$\tau_{r\beta}^{tot} = \frac{C}{r^2}, \quad (3.8)$$

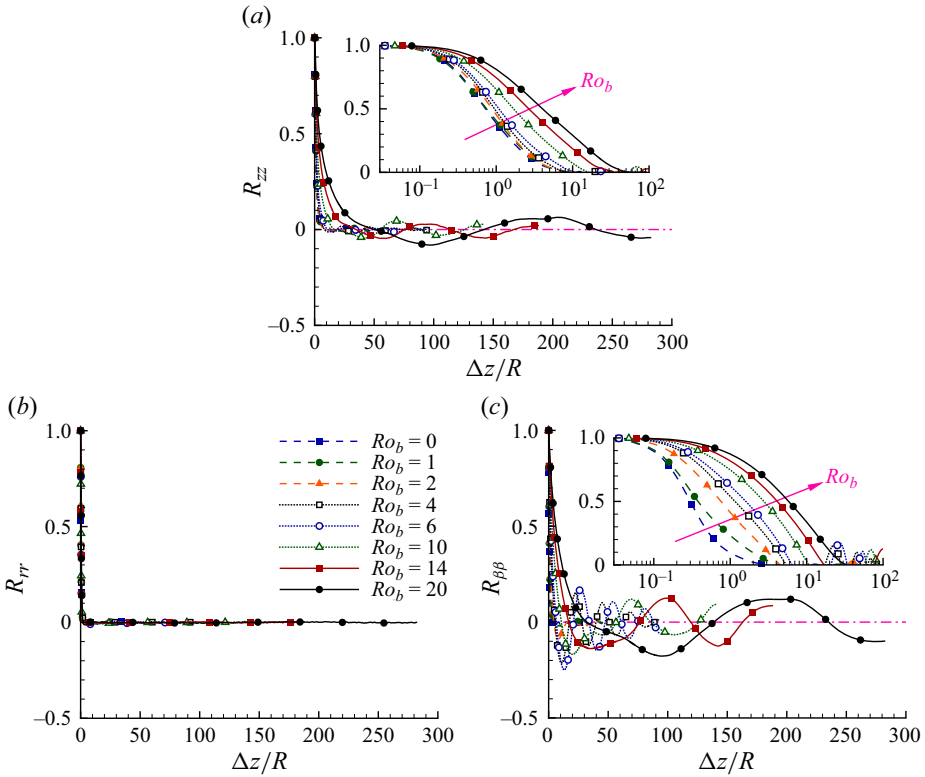


Figure 9. Profiles of two-point autocorrelation coefficients (a) axial component  $R_{zz}$ , (b) radial component  $R_{rr}$  and (c) azimuthal component  $R_{\beta\beta}$  for the eight test cases of different rotation numbers  $Ro_b$ , calculated along the streamwise direction at wall-normal position  $y = 0.083$  (or  $y^+ \approx 15$ ). Pink arrows in the partially enlarged panels (a,c) indicate the direction of an increasing rotation number. Results are based on test cases of the longest pipes at corresponding rotation numbers listed in table 1.

where  $C$  is a constant. The regularity condition at the pipe centre requires that  $C \equiv 0$ . As such,

$$\tau_{r\beta}^{tot} \equiv 0 \quad \text{and} \quad \tau_{r\beta}^{vis} \equiv \langle u'_r u'_\beta \rangle, \quad (3.9a,b)$$

hold rigorously in an axially rotating pipe flow. This is an interesting result, which indicates that the total  $r-\beta$  shear stress is zero identically, such that the viscous shear stress is always balanced by the turbulent shear stress (in an  $r-\beta$  plane) at all rotation numbers. This mechanism gives an analytical explanation to the mirror effect between the profiles of  $\tau_{r\beta}^{vis+}$  and  $-\langle u'_r u'_\beta \rangle^+$  as observed in figure 8(b).

### 3.4. Two-point correlations and spectral analysis

Figure 9 compares the two-point autocorrelation coefficients of three velocity components  $R_{zz}$ ,  $R_{rr}$  and  $R_{\beta\beta}$  at different rotation numbers based on the eight test cases of table 1. All coefficients are determined along the axial direction at wall-normal position  $y^+ \approx 15$ , where Reynolds stress component  $\langle u'_z u'_z \rangle^+$  peaks in the context of a non-rotating pipe flow. The two-point autocorrelation coefficient is defined as

$$R_{ii}(\Delta z) = \frac{\langle u'_i(r, \beta, z, t) u'_i(r, \beta, z + \Delta z, t) \rangle}{\langle u'_i(r, \beta, z, t) u'_i(r, \beta, z, t) \rangle}, \quad (3.10)$$

where  $i$  indicates the three directions (i.e.  $r$ ,  $\beta$  and  $z$ ) of the cylindrical coordinate system, and no summation convention is implied in this equation. In figure 9(a,c), a partially enlarged panel is also displayed in a semi-logarithmic coordinate in order to clearly display the variations of  $R_{zz}$  and  $R_{\beta\beta}$  for smaller two-point separations ( $\Delta z/R$ ). From figure 9(b), it is apparent that the profiles of the radial two-point autocorrelation coefficient  $R_{rr}$  at all rotation numbers approach zero rather rapidly as the two-point separation  $\Delta z/R$  increases. By contrast, the axial and azimuthal two-point correlation coefficients  $R_{zz}$  and  $R_{\beta\beta}$  shown in figure 9(a,c) are more sensitive to the rotation number, as their values increase monotonically with an increasing value of  $Ro_b$  for small two-point separations. Furthermore, it is very interesting to observe a quasi-periodical pattern in the profiles of  $R_{zz}$  and  $R_{\beta\beta}$  in figures 9(a) and 9(c), respectively. The spatial periods become larger as the rotation number  $Ro_b$  increases. It is evident that the axial scales of the most energetic secondary flow structures (i.e. Taylor columns) induced by the Coriolis force increase monotonically as the rotation number is increased. The quasi-periodical patterns in the profiles of  $R_{zz}$  and  $R_{\beta\beta}$  are most apparent at high rotation numbers.

As mentioned earlier, there are two main types of flow structure in an axially rotating pipe flow. The first type is streaky structures near the wall (or hairpins) that are typical of the turbulent boundary layer of a pipe flow (rotating or not). The second type is Taylor columns similar to those observed in rotating isotropic turbulence (see, e.g., Bartello *et al.* 1994; Gallet 2015; van Kan & Alexakis 2020; Pestana & Hickel 2020). However, compared with rotating isotropic turbulence, a turbulent pipe flow is bounded peripherally by the pipe wall of curvature  $1/R$ . From the profiles of  $R_{zz}$  and  $R_{\beta\beta}$ , it is inferred that the Taylor columns in an axially rotating pipe flow exhibit a spiral pattern, which elongate in the axial direction and spin in the azimuthal direction. In fact, the axial quasi-periodicity of the two-point autocorrelation ( $R_{\beta\beta}$ ) observed in figure 9(c) is a consequence of the counterclockwise spinning motion of Taylor columns demonstrated previously in figures 3, 4(a) and 5(b). Furthermore, both axial and azimuthal motions of Taylor columns are quasi-periodic in the axial direction, which are evident in figure 9(a,c). A vivid analogy for describing the instantaneous shape of Taylor columns in an axially rotating pipe flow is ‘a bundle of hemp ropes’, twisted together with many smaller individual ropes of different brand names (as such, each can have its own axial and azimuthal periods). As turbulence structures, small Taylor columns can be destroyed by dissipation and transported by diffusion and convection in a viscous flow.

The analysis of Taylor columns can be refined through a spectral analysis, which will show that Taylor columns have two characteristic axial length scales. To demonstrate, figure 10 compares the profiles of the premultiplied axial spectra of axial, radial and azimuthal velocity fluctuations (i.e.  $k_z^+ \tilde{E}_{zz}^+$ ,  $k_z^+ \tilde{E}_{rr}^+$  and  $k_z^+ \tilde{E}_{\beta\beta}^+$ , respectively) of the eight test cases of the longest pipes of table 1. All profiles are calculated at wall-normal position  $y^+ \approx 15$ , where the axial Reynolds normal stress peaks in the context of a non-rotating pipe flow. The 1-D axial energy spectrum of velocity fluctuations is defined as

$$\tilde{E}_{ii}(k_z) = \text{Re} \left\{ \overline{\widehat{u}_i^* \widehat{u}_i} \right\}, \quad (3.11)$$

where the index  $i$  denotes  $r$ ,  $\beta$  or  $z$  of the cylindrical coordinate system, and no summation convention is implied. An overbar represents temporal averaging. The operator  $\text{Re}\{\cdot\}$  and superscript  $*$  denote the real part and conjugate of a complex number, respectively. A hat denotes Fourier transform in the axial direction of an arbitrary variable  $\phi(r, \beta, k_z, t)$ , i.e.

$$\hat{\phi}(r, \beta, k_z, t) = \frac{1}{L_z} \int_0^{L_z} \phi(r, \beta, z, t) e^{-ik_z z} dz, \quad (3.12)$$

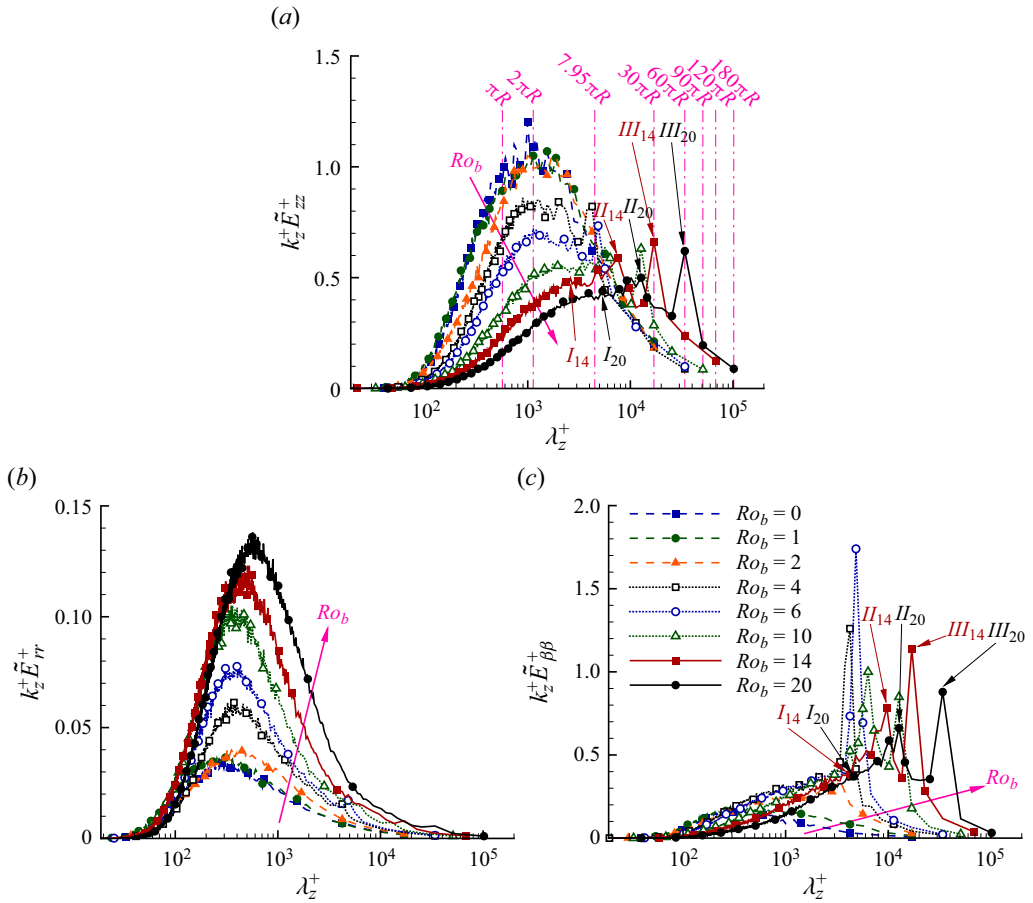


Figure 10. Profiles of premultiplied (a) axial  $k_z^+ \tilde{E}_{zz}^+$ , (b) radial  $k_z^+ \tilde{E}_{rr}^+$  and (c) azimuthal  $k_z^+ \tilde{E}_{\beta\beta}^+$  velocity spectra at eight different rotation numbers for  $Ro_b = 0-20$ , calculated along the streamwise direction at wall-normal position  $y = 0.083$  (or  $y^+ \approx 15$ ). Pink arrow points to the direction of an increasing rotation number. For clarity, the peaks of premultiplied spectra ( $I$ ,  $II$  and  $III$ ) are labelled only for the two highest rotation numbers  $Ro_b = 14$  and  $20$ . Results are based on test cases of the longest pipes at corresponding rotation numbers listed in [table 1](#).

where  $\mathbf{i} = \sqrt{-1}$  is the imaginary unit and  $k_z = n_z k_{0z}$  is the axial wavenumber, with  $n_z \in [-N_z/2, N_z/2 - 1]$  being an integer and  $k_{z0} = 2\pi/L_z$  being the smallest positive wavenumber. The axial wavelength is defined as  $\lambda_z = 2\pi/k_z$ , non-dimensionalised as  $\lambda_z^+ = \lambda_z u_\tau / \nu$ .

For the premultiplied axial velocity spectrum  $k_z^+ \tilde{E}_{zz}^+$ , it is evident in [figure 10\(a\)](#) that the mode of its dome peak (corresponding to the characteristic length scale of the most energetic eddies) of the non-rotating pipe flow ( $Ro_b = 0$ ) is located within  $\lambda_z^+ \in [530, 2450]$  at  $y^+ \approx 15$  in the near-wall region, where axial Reynolds normal stress peaks. This peak of  $k_z^+ \tilde{E}_{zz}^+$  is a consequence of near-wall streaks of the boundary layer developing over the pipe wall. The formation of this peak does not rely on axial system rotation, but rather, it is a characteristic of a turbulent boundary layer commonly found in wall-bounded flows over flat plates (see, e.g., [Zhou et al. 1999](#); [Adrian 2007](#); [Wu & Moin 2009](#)) or in non-rotating pipe flows (see, e.g., [Wu & Moin 2008](#); [Wu et al. 2012](#); [Baltzer, Adrian & Wu](#)



2013). This peak of the premultiplied axial velocity spectrum  $k_z^+ \tilde{E}_{zz}^+$  is denoted as peak ‘I’ hereafter, and for a specific rotation number (e.g.  $Ro_b = 14$  or  $20$ ), it is indicated using the rotation number as the subscript (as  $I_{14}$  or  $I_{20}$ , respectively). As the rotation number is increased from  $Ro_b = 0$  to  $20$ , the magnitude of the first peak (I) of  $k_z^+ \tilde{E}_{zz}^+$  decreases monotonically. Meanwhile, the mode of the first peak moves towards larger wavelengths, leading to an increasingly broadband vortical scales in the axial direction as the rotation number is increased. At the highest rotation number  $Ro_b = 20$ , the wavelengths of the first peak range within  $\lambda_z^+ \in [4840, 5660]$ .

From figure 10(a), it is interesting to see that at high rotation numbers (for  $Ro_b \geq 10$ ), there are two additional peaks (denoted as peaks ‘II’ and ‘III’) in addition to peak I in the profiles of the premultiplied axial velocity spectrum  $k_z^+ \tilde{E}_{zz}^+$ . Similarly, peaks of different rotation numbers are differentiated symbolically by using rotation numbers as the subscripts (e.g.  $II_{20}$  or  $III_{20}$  for the case of  $Ro_b = 20$ ). The appearance of peaks II and III in the profiles of  $k_z^+ \tilde{E}_{zz}^+$  is due to the presence of Taylor columns, which are elongated in the axial direction and spin in the azimuthal direction, as discussed previously through the analysis of two-point autocorrelation coefficients  $R_{zz}$  and  $R_{\beta\beta}$  associated with figures 9(a) and 9(c), respectively. Using the examples of  $Ro_b = 14$  and  $20$ , the peak magnitudes follow an ascending order, i.e. ‘ $I_{14} < II_{14} < III_{14}$ ’ and ‘ $I_{20} < II_{20} < III_{20}$ .’ This indicates that at high rotation numbers, the share of TKE held by Taylor columns associated with peaks II and III (and especially with peak III) is much larger than that held by streaks at this radial position. Within the range of the rotation numbers tested here, all three peaks of  $k_z^+ \tilde{E}_{zz}^+$  have been well captured. The premultiplied energy spectrum loss (in terms of the percentage of its peak value) is less than 20 % at their cutoff wavelengths. It is also interesting to observe that there is no apparent distinction between the second and third peaks at moderate rotation numbers of  $Ro_b = 4$  and  $6$ , as the two types (axial and azimuthal) of structures of Taylor columns are still evolving temporally and spatially. This indicates that Taylor columns start to occur at moderate rotation numbers with similar characteristic axial wavelengths. However, as the rotation number continues to increase, Taylor columns evolve spatially to feature two distinct axial characteristic wavelengths, corresponding to modal values of peaks II and III of  $k_z^+ \tilde{E}_{zz}^+$ . Furthermore, both characteristic axial wavelengths of Taylor columns increase as the rotation number is increased.

Given that the characteristic axial length scale of energetic eddy motions grows with an increasing rotation number, the pipe length is extended from  $L_z = 30\pi R$  to  $180\pi R$  as rotation number increases from  $Ro_b = 0$  to  $20$  (see table 1). As shown in figure 10(a), the cutoff wavelength varies from  $(\lambda_z^+)_{CF} = 16964.6$  at  $Ro_b = 0$  to  $(\lambda_z^+)_{CF} = 101787.6$  at  $Ro_b = 20$ . At the cutoff wavelength, the premultiplied energy spectrum loss varies from 10.33 % at  $Ro_b = 4$  to 19.81 % at  $Ro_b = 1$ . Clearly, if the short pipe of  $L_z = 25R$  (or  $7.958\pi R$ ) is used (as in Orlandi & Ebstein 2000), the prediction of the largest peak  $III_{20}$  of  $k_z^+ \tilde{E}_{zz}^+$  that is characteristic of Taylor columns would be missed entirely. It should be indicated that it is neither necessary nor realistic to fully prevent premultiplied energy spectrum loss at the cutoff wavelength in either a DNS or an experiment, as it implies usage of a pipe of infinite length. Furthermore, flow structures of large wavelengths far beyond the mode of the premultiplied spectrum typically possess very low TKE. However, it is important to ensure that all dominant modes of premultiplied spectra are captured in a DNS, LES or physical experiment, which correspond to the characteristic length scales of the most energetic eddy motions. In practice, for example, the premultiplied energy spectrum loss at the cutoff wavelength is often kept lower than 5/8 or 3/8 of its modal value (i.e.  $0.625 \max(k_z^+ \tilde{E}_{ii}^+)$  or  $0.375 \max(k_z^+ \tilde{E}_{ii}^+)$ ) for moderate and relatively high-precision

requirements, respectively) in DNS studies of turbulent plane-channel flows (Hoyas & Jiménez 2006; Avsarkisov *et al.* 2014; Yang & Wang 2018; Bagheri, Wang & Yang 2020).

In contrast to the general trend of the premultiplied axial velocity spectrum  $k_z^+ \tilde{E}_{zz}^+$  shown in figure 10(a), the magnitude of the premultiplied radial velocity spectrum  $k_z^+ \tilde{E}_{rr}^+$  increases monotonically as the rotation number is increased, a pattern that is apparent in figure 10(b). The presence of the dominant peak of  $k_z^+ \tilde{E}_{rr}^+$  at this near-wall position of approximately  $y^+ = 15$  results from the streaky structures. As shown in figure 10(b), the modal position of  $k_z^+ \tilde{E}_{rr}^+$  is relatively stable at all eight rotation numbers tested. A careful perusal of the figure indicates that the characteristic axial length scale of the most energetic radial eddy motions as indicated by the mode of  $k_z^+ \tilde{E}_{rr}^+$  increases from  $\lambda_z^+ = 282.74$  to 568.65 as the rotation number is increased from  $Ro_b = 0$  to 20.

Figure 10(c) compares the premultiplied azimuthal velocity spectrum  $k_z^+ \tilde{E}_{\beta\beta}^+$  at eight rotation numbers. Similar to figure 10(a), the number of peaks in the profile of  $k_z^+ \tilde{E}_{\beta\beta}^+$  varies with the rotation number. At low rotation numbers  $Ro_b = 0$  and 1, the profile of  $k_z^+ \tilde{E}_{\beta\beta}^+$  shows only one dominant peak (denoted as  $I_0$  and  $I_1$ , respectively, not labelled in the figure) within the range of  $\lambda_z^+ \in [220, 600]$ , which is a signature of near-wall streaks, shown also at higher rotation numbers at slightly larger wavelengths. However, at moderately high rotation numbers of  $Ro_b = 4$  and 6 as shown in figure 10(c), a second sharp peak (denoted as  $II_4$  and  $II_6$ , respectively, not labelled in the figure) appears around  $\lambda_z^+ = 4241$  and 4847, which is an indication of the occurrence of Taylor columns. As the rotation number continues to increase, Taylor columns further develop in both axial and azimuthal directions leading to two characteristic axial wavelengths. At higher rotation numbers for  $Ro_b \geq 10$ , two dominant peaks ( $II$  and  $III$ ) of Taylor columns (besides the existing reduced peak  $I$  of the streaks) are identified. At the two highest rotation numbers tested, these two characteristic peaks of Taylor columns are labelled as  $II_{14}$  and  $III_{14}$  (at  $Ro_b = 14$ ) and  $II_{20}$  and  $III_{20}$  (at  $Ro_b = 20$ ) in figure 10(c). By comparing figures 10(a) and 10(c), it is clear that the pipe flow motion is dominated by streaks (or hairpins, signified by peak  $I$ ) at low rotation numbers for  $Ro_b \in [0, 2]$ , Taylor columns of one single characteristic wavelength (signified by peak  $II$ ) at moderate rotation numbers for  $Ro_b \in [4, 6]$  and Taylor columns of two characteristic wavelengths (signified by peaks  $II$  and  $III$ ) at high rotation numbers for  $Ro_b \in [10, 20]$ . The two peaks ( $II$  and  $III$ ) of  $k_z^+ \tilde{E}_{zz}^+$  and  $k_z^+ \tilde{E}_{\beta\beta}^+$  observed at the high rotation numbers for  $Ro_b \geq 10$  are consistent with the quasi-periodic behaviours of  $R_{zz}$  and  $R_{\beta\beta}$  observed previously in figure 9(a,c).

Thus far, the analysis of the axial premultiplied velocity spectra has been conducted at  $y = 0.083$  (or  $y^+ \approx 15$ ) in the near-wall region of the pipe in figure 10. From the previous analysis of figure 7(a), it was observed that the value of  $\langle u'_z u'_z \rangle^+$  peaks at this wall-normal position at  $Ro_b = 0$ , but at  $y = 0.566$  (or  $y^+ \approx 102$ ) at  $Ro_b = 20$ . It would be interesting to further examine the behaviours of the three components of the axial premultiplied velocity spectra at this special wall-normal position of  $y = 0.566$ , which is demonstrated in figure 11. From this figure, it is seen that all dominant peaks of the axial premultiplied velocity spectra (e.g. peaks  $I_{14}$ ,  $II_{14}$  and  $III_{14}$  for  $Ro_b = 14$ , peaks  $I_{20}$ ,  $II_{20}$  and  $III_{20}$  for  $Ro_b = 20$ ) have been well captured based on the eight test cases of the longest pipes listed in table 1. As shown in figure 11(a), the largest premultiplied energy spectrum loss is about 21.37% (in terms of the percentage of its peak value) at  $Ro_b = 1$  at the cutoff wavelength.

By comparing figure 11 with figure 10, it is clear that the profile patterns of all three components of the axial premultiplied velocity spectra change considerably as the elevation increases from  $y = 0.083$  to 0.566. As shown in figure 11(a), the magnitudes

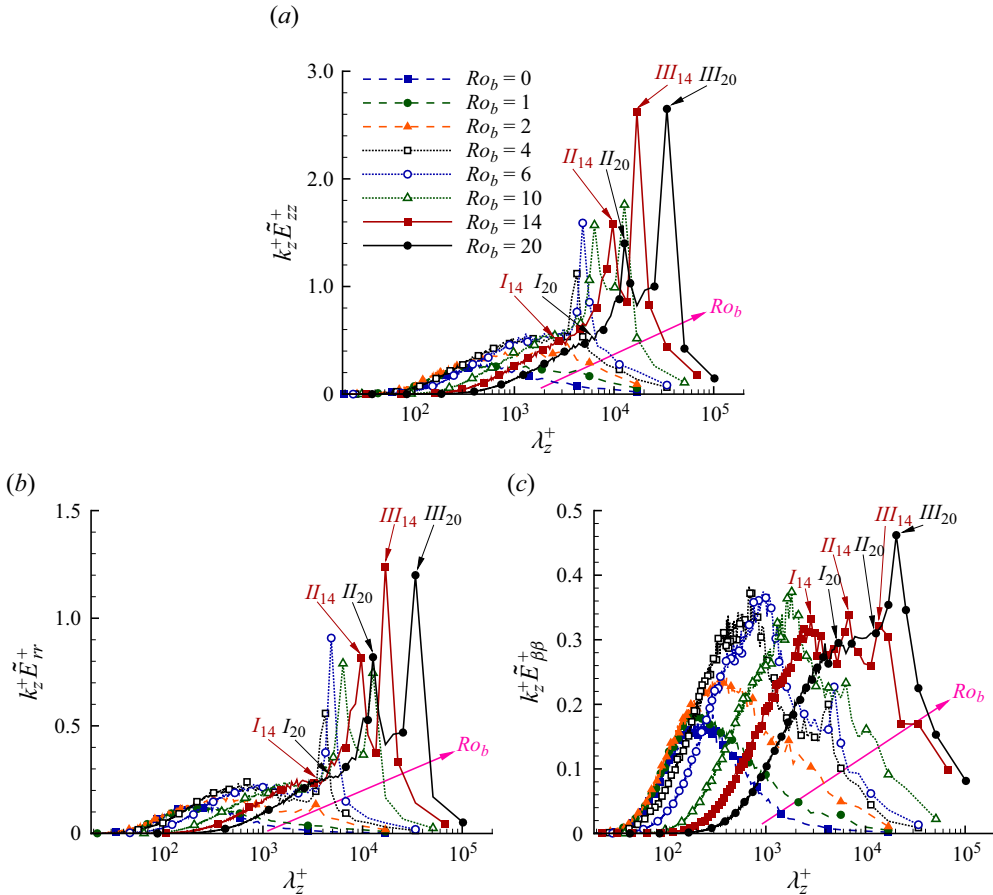


Figure 11. Profiles of premultiplied (a) axial  $k_z^+ \tilde{E}_{zz}^+$ , (b) radial  $k_z^+ \tilde{E}_{rr}^+$  and (c) azimuthal  $k_z^+ \tilde{E}_{\beta\beta}^+$  velocity spectra at eight different rotation numbers for  $Ro_b = 0-20$ , calculated along the streamwise direction at wall-normal position  $y = 0.566$  (or  $y^+ \approx 102$ ). For clarity, the peaks of premultiplied spectra ( $I$ ,  $II$  and  $III$ ) are labelled only for the two highest rotation numbers  $Ro_b = 14$  and  $20$ . Results are based on test cases of the longest pipes at corresponding rotation numbers listed in [table 1](#).

of peaks  $II$  and  $III$  of  $k_z^+ \tilde{E}_{zz}^+$  are significantly larger than that of peak  $I$  at higher rotation numbers of  $Ro_b \geq 10$ . This indicates that Taylor columns become increasingly energetic as the distance from the pipe wall increases. Such trend of Taylor columns is more clearly reflected in the profiles of all three axial premultiplied spectra. As shown in [figure 10\(b\)](#), the profile of  $k_z^+ \tilde{E}_{rr}^+$  has only one dominant peak in the near-wall region (at  $y = 0.083$ ), which is peak  $I$  resulted from near-wall streaks of the boundary layer developing over the pipe wall. By contrast, as is evident in [figure 11\(b\)](#), the profile of  $k_z^+ \tilde{E}_{rr}^+$  is dominated by peaks  $II$  and  $III$  of Taylor columns at moderate and high rotation numbers of  $Ro_b \geq 4$  at a higher elevation of  $y = 0.566$ . In comparison with the profiles of  $k_z^+ \tilde{E}_{\beta\beta}^+$  in the near-wall region shown in [figure 10\(c\)](#), those shown in [figure 11\(c\)](#) indicate that the magnitudes of peaks  $II$  and  $III$  reduce relative to that of peak  $I$  as the elevation increases from  $y = 0.083$  to  $0.566$ .

[Figure 12](#) shows the profiles of the three components of the axial premultiplied velocity spectra at the pipe centre ( $y = 1.0$ ) where the mean axial velocity value reaches the maximum and the magnitudes of Reynolds normal stresses  $\langle u'_r u'_r \rangle$  and  $\langle u'_\beta u'_\beta \rangle$  are the

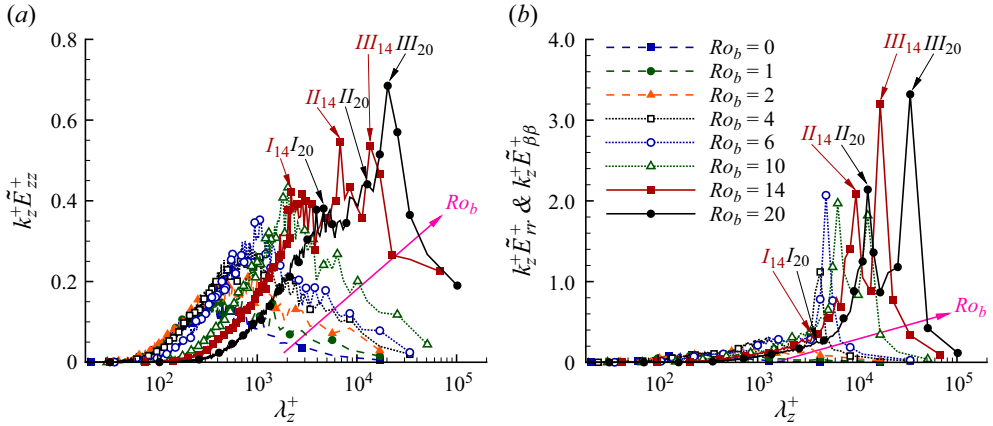


Figure 12. Profiles of premultiplied (a) axial  $k_z^+ \tilde{E}_{zz}^+$ , (b) radial  $k_z^+ \tilde{E}_{rr}^+$  and (c) azimuthal  $k_z^+ \tilde{E}_{\beta\beta}^+$  velocity spectra at eight different rotation numbers for  $Ro_b = 0-20$ , calculated along the streamwise direction at the pipe centre  $y = 1.0$ . For clarity, the peaks of premultiplied spectra ( $I$ ,  $II$  and  $III$ ) are labelled only for the two highest rotation numbers  $Ro_b = 14$  and  $20$ . Results are based on test cases of the longest pipes at corresponding rotation numbers listed in table 1.

maximum. At the pipe centre,  $k_z^+ \tilde{E}_{rr}^+ \equiv k_z^+ \tilde{E}_{\beta\beta}^+$ . Clearly, all dominant peaks of  $k_z^+ \tilde{E}_{zz}^+$ ,  $k_z^+ \tilde{E}_{rr}^+$  and  $k_z^+ \tilde{E}_{\beta\beta}^+$  have been well captured at eight rotation numbers based on test cases of the longest pipes listed in table 1. In comparison with figures 10 and 11, it is clear that the peak magnitude of  $k_z^+ \tilde{E}_{zz}^+$  shown in figure 12 drops as the elevation increases from  $y = 0.083$  to  $1.0$ . Furthermore, it is clear that the profile of  $k_z^+ \tilde{E}_{\beta\beta}^+$  features peak  $I$  of hairpins in non-rotating or slowly rotating pipe flows (of low rotation numbers  $Ro_b = 0-2$ ). However, as the rotation number increases, the profile of  $k_z^+ \tilde{E}_{\beta\beta}^+$  begins to signify Taylor columns, featuring one single dominant peak  $II$  at moderate rotation numbers (of  $Ro_b = 4-6$ ) but two dominant peaks  $II$  and  $III$  at high rotation numbers (of  $Ro_b \geq 10$ ).

Figure 13 compares the contour patterns of the non-dimensionalised premultiplied 1-D spectrum of axial velocity fluctuations  $k_z^+ \tilde{E}_{zz}^+$  as a function of  $\lambda_z^+$  and  $y^+$  at two rotation numbers  $Ro_b = 0$  and  $20$  based on the longest-pipe cases of table 1. The effects of axial system rotation on the generation of Taylor columns are evident by directly contrasting figures 13(a) against 13(b). For the non-rotating pipe flow, there is only one mode located at  $(\lambda_z^+, y^+) = (997.4, 12.9)$ , which corresponds to peak  $I_0$ . This peak is a consequence of near-wall streaks. However, at the highest rotation number  $Ro_b = 20$  as shown in figure 13(b), the presence of all three peaks ( $I_{20}$ ,  $II_{20}$  and  $III_{20}$ ) are evident, located at  $(\lambda_z^+, y^+) = (7268.5, 63.8)$ ,  $(12719.9, 114.3)$  and  $(33919.8, 97.6)$ , respectively. In figure 13(a), three regions of high-, intermediate- and low-intensity cores are distinguished by different colours enclosed within three isopleths, corresponding to  $0.875 \max(k_z^+ \tilde{E}_{zz}^+)$ ,  $0.625 \max(k_z^+ \tilde{E}_{zz}^+)$  and  $0.375 \max(k_z^+ \tilde{E}_{zz}^+)$  (or  $7/8$ ,  $5/8$  and  $3/8$  of the peak value of  $k_z^+ \tilde{E}_{zz}^+$ , respectively). The high-intensity core within the innermost isopleth of  $0.875 \max(k_z^+ \tilde{E}_{zz}^+)$  are associated with the most energetic eddies of the turbulent flow field. Although the low-intensity core enclosed by the outermost isopleth of  $0.375 \max(k_z^+ \tilde{E}_{zz}^+)$  corresponds to less-dominant energetic eddies consisting of a wide range wavelengths, it still makes a considerable contribution to the total TKE. Because the TKE is mostly held by Taylor columns at the high rotation number  $Ro_b = 20$ , the magnitude of peak  $I_{20}$  is

## DNS of turbulent pipe flow subjected to axial rotation

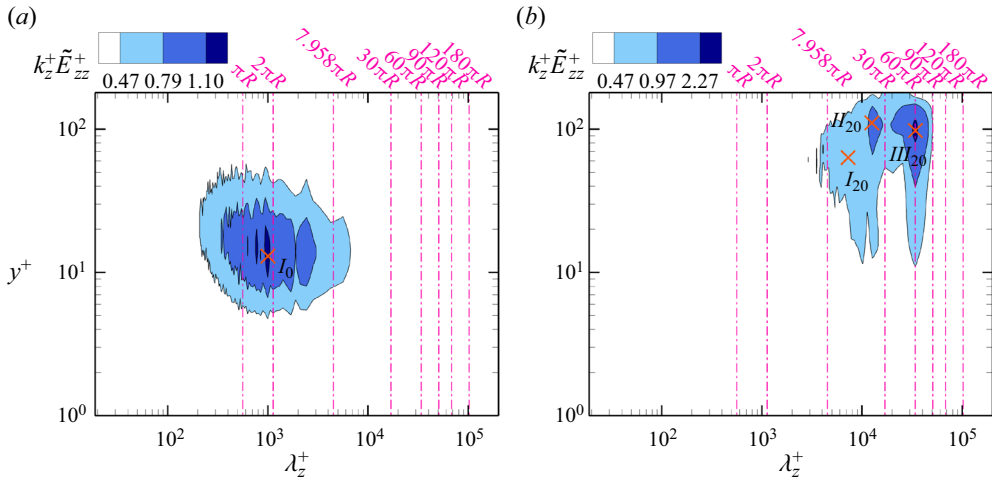


Figure 13. Isopleths of premultiplied axial velocity spectra  $k_z^+ \tilde{E}_{zz}^+$  with respect to wall-normal coordinate  $y^+$  and wavelength  $\lambda_z^+$  for the (a) non-rotating ( $Ro_b = 0$ ) and (b) axially rotating ( $Ro_b = 20$ ) pipe flows. The cross symbols ‘ $\times$ ’ demarcate the locations of the three peaks *I*, *II* and *III*. The three energy levels are distinguished by the innermost, intermediate and outermost isopleths of 87.5 %, 62.5 % and 37.5 % of the peak value  $\max(k_z^+ \tilde{E}_{zz}^+)$  in panel (a), and 87.5 %, 37.5 % and 18.0 % of the peak value  $\max(k_z^+ \tilde{E}_{zz}^+)$  in panel (b), respectively.

much less than those of peaks *II*<sub>20</sub> and *III*<sub>20</sub>. Therefore, the value of the outermost isopleth is reduced to 0.18  $\max(k_z^+ \tilde{E}_{zz}^+)$  in order to have a clear view of the location of peak *I*<sub>20</sub>. By comparing figures 13(a) and 13(b), it is also seen that the modal position of all three peaks (*I*<sub>20</sub>, *II*<sub>20</sub> and *III*<sub>20</sub>) are near the pipe centre. At the rotation number is increased from  $Ro_b = 0$  to 20, the modal position of peak *I* increases from  $y^+ = 12.9$  to 63.8.

Figure 14 compares the profiles of  $k_z^+ \tilde{E}_{zz}^+$  of  $Ro_b = 20$  at five wall-normal distances ranging from  $y = 0.083$  (near the wall) to  $y = 1.0$  (at the pipe centre). The results are based on the case of the longest pipe  $L_z = 180\pi R$ . At this high rotation number, it is clear that turbulent flow structures of an axially rotating pipe flow feature predominantly Taylor columns (as indicated by peaks *II*<sub>20</sub> and *III*<sub>20</sub>). From the previous analysis of figures 10–12, it is understood that the modal wavelengths corresponding to peaks *I*, *II* and *III* of profiles of  $k_z^+ \tilde{E}_{zz}^+$ ,  $k_z^+ \tilde{E}_{rr}^+$  and  $k_z^+ \tilde{E}_{\beta\beta}^+$  may vary with wall-normal distance  $y$ . As is evident in figure 14(a–c), the characteristic wavelength corresponding to peak *II*<sub>20</sub> is rather stable (with  $\lambda_z^+ \approx 12723$ ) as the elevation ( $y$  value) varies. However, the characteristic wavelengths of peaks *I*<sub>20</sub> and *III*<sub>20</sub> range slightly, which are indicated by a pair of dashed lines and arrows in figure 14(a–c). A careful perusal of figure 14(a,c) indicates that the magnitudes of  $k_z^+ \tilde{E}_{zz}^+$  and  $k_z^+ \tilde{E}_{\beta\beta}^+$  are the largest and the smallest, respectively, at  $y = 0.566$ , which are consistent with the previous observations of a local maximum value of  $\langle u'_z u'_z \rangle^+$  and a local minimum value of  $\langle u'_\beta u'_\beta \rangle^+$  in figure 7(a,c) at a similar wall-normal position, respectively. In figure 14(b), it is shown that the magnitude of  $k_z^+ \tilde{E}_{rr}^+$  increases as  $y$  increases. Such general monotonic trend is consistent with that of  $\langle u'_r u'_r \rangle^+$  observed in figure 7(b). This is an expected feature, simply because the Reynolds stresses relate directly to their premultiplied spectra  $k_z \tilde{E}_{ij}$  through integration  $\langle u'_i u'_i \rangle = 2 \int_0^\infty k_z \tilde{E}_{ij} d(\ln k_z)$ .

### 3.5. Higher-order turbulence statistics

So far, the influence of the Coriolis force on an axially rotating pipe flow has been studied thoroughly through investigations into the mean flow and second-order turbulence

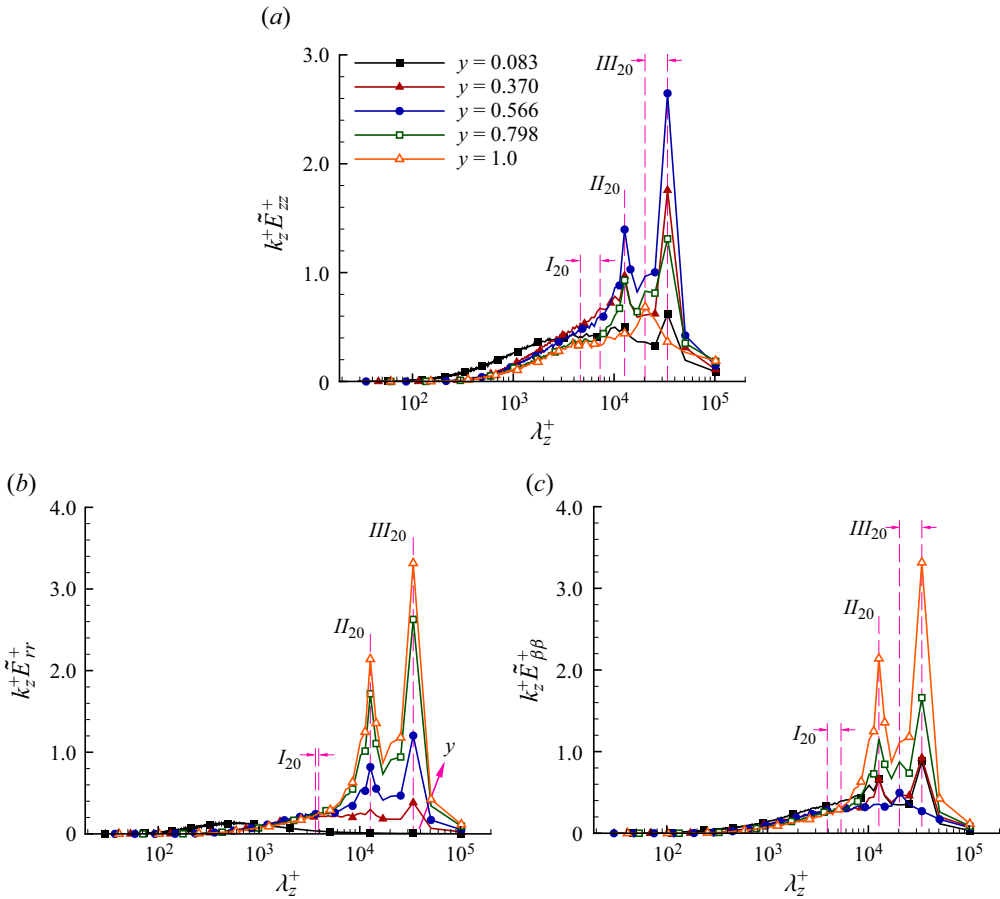


Figure 14. Profiles of premultiplied (a) axial  $k_z^+ \tilde{E}_{zz}^+$ , (b) radial  $k_z^+ \tilde{E}_{rr}^+$  and (c) azimuthal  $k_z^+ \tilde{E}_{\beta\beta}^+$  velocity spectra at the highest rotation number  $Ro_b = 20$ , calculated along the streamwise direction at different wall-normal ( $y$ ) positions, based on the test case of the longest pipe  $L_z = 180\pi R$ .

statistics. In order to develop a deeper insight into the flow, the third- and fourth-order statistical moments can be further examined. Figure 15 shows the radial profiles of the skewness and flatness factors of three velocity fluctuations, defined as

$$S(u'_i) = \frac{\langle u_i'^3 \rangle}{\langle u_i'^2 \rangle^{3/2}} \quad \text{and} \quad F(u'_i) = \frac{\langle u_i'^4 \rangle}{\langle u_i'^2 \rangle^2}, \quad (3.13a,b)$$

respectively. Here, indices  $i = 1, 2$  and  $3$ , correspond to cylindrical coordinates  $r, \beta$  and  $z$ , respectively, and no summation convention is implied. To study the ejection and sweep events in a circular pipe flow, it is convenient to consider the analogy of a boundary-layer flow developing over a flat plate. Thus, the negative of instantaneous radial velocity fluctuation ( $-u'_r$ ) is used in the calculation of the radial skewness factor  $S(-u'_r)$ . This greatly facilitates an intuitive near-wall analysis of physical phenomena associated with the skewness factor based on the non-dimensional wall coordinate  $y$ .

Figure 15(a) compares the profiles of the axial skewness factor  $S(u'_z)$  at different rotation numbers. Clearly, the value of  $S(u'_z)$  drops rapidly in the near-wall region. For a non-rotating pipe flow, the axial skewness factor has a zero-crossing point at  $y = 0.068$



DNS of turbulent pipe flow subjected to axial rotation

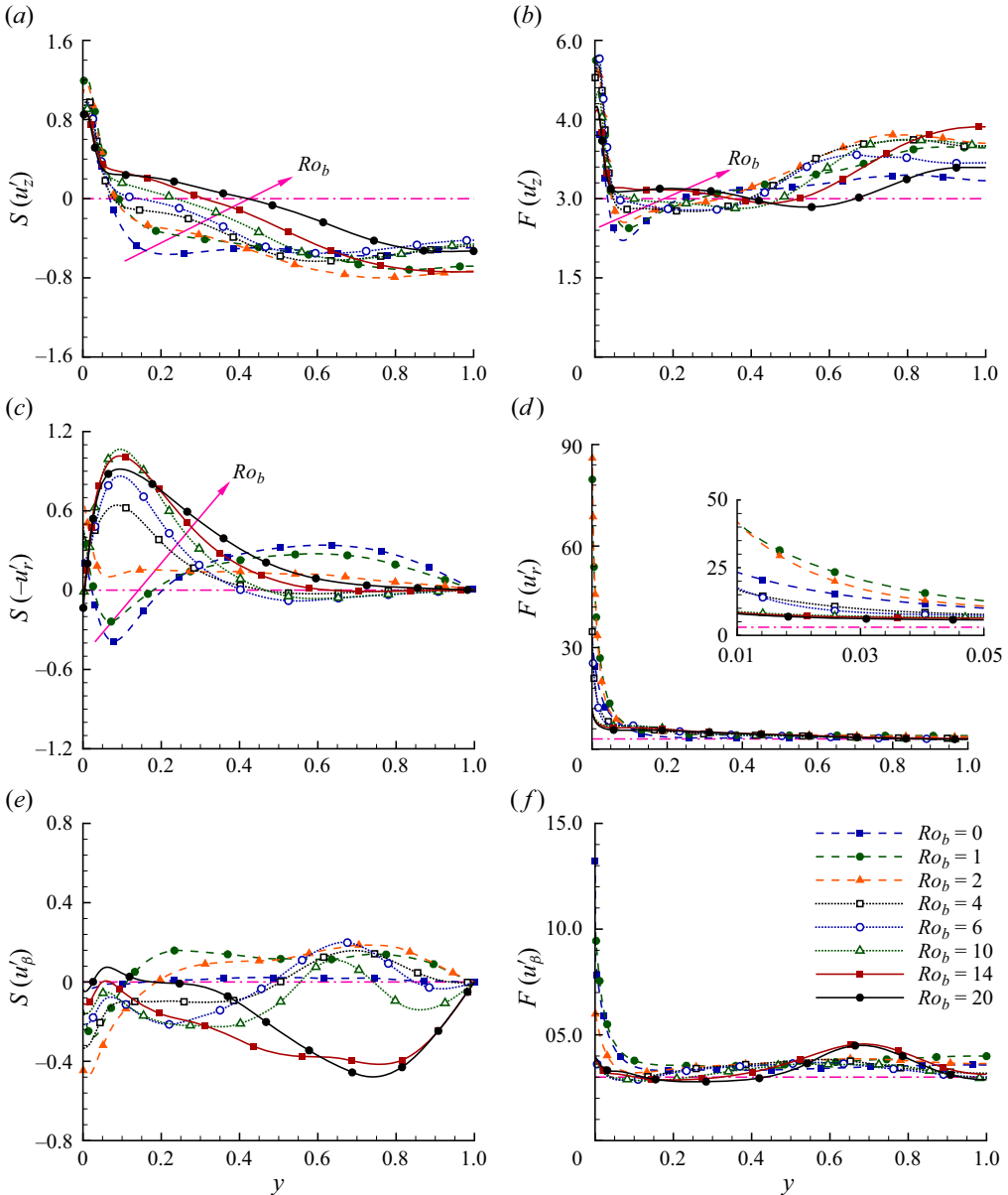


Figure 15. Profiles of skewness (a,c,e) and flatness factors (b,d,f) of three velocity fluctuations at various rotation numbers of  $Ro_b = 0-20$ : (a)  $S(u'_z)$ ; (b)  $F(u'_z)$ ; (c)  $S(-u'_r)$ ; (d)  $F(u'_r)$ ; (e)  $S(u'_\beta)$ ; (f)  $F(u'_\beta)$ . The pink dash-dotted line indicates the theoretical values of an ideal Gaussian distribution, which are 0 and 3 for skewness and flatness, respectively. The pink arrow shows a local trend of an increasing rotation number  $Ro_b$ . Results are based on test cases of the longest pipes at corresponding rotation numbers listed in table 1.

(in the near-wall region of the pipe), and then holds its magnitude almost constant with  $S(u'_z) > -0.6$  as the wall-normal distance increases, which is consistent with the observation of Eggels *et al.* (1994) on non-rotating pipe flows. As soon as the axial rotation is imposed, this pattern of  $S(u'_z)$  is broken and the zero-crossing position is shifted towards the pipe centre. At  $Ro_b = 20$ , the  $S(u'_z)$  profile crosses zero at a much high elevation (of  $y = 0.422$ ) from the wall. In figure 15, although a strict general monotonic trend in the

profiles of skewness and flatness factors with respect to a varying rotation number is not observed, arrows are still plotted wherever a clear local monotonic trend can be identified in the profiles. As is evident in [figure 15\(c\)](#), the radial skewness factor  $S(-u'_r)$  has two zero-crossing points at  $y = 0.023$  and  $y = 0.203$  in the near-wall region. A negative peak value can be observed at  $y = 0.078$  with  $S(-u'_r) = -0.386$  at  $Ro_b = 0$ . However, as the rotating effect intensifies, the negative peak of  $S(-u'_r)$  transitions progressively to become a positive peak. At  $Ro_b = 10$ , the radial skewness factor reaches its maximum of  $S(-u'_r) = 1.066$  at  $y = 0.093$ , and the two zero-crossing points occur at  $y = 0.003$  and  $y = 0.468$ . At the highest rotation number  $Ro_b = 20$ , the profile of  $S(-u'_r)$  crosses zero at  $y = 0.005$  and the profile of  $S(-u'_r)$  maintains positively valued in most of the regions. From [figure 15\(e\)](#), it is evident that the azimuthal skewness factor basically follows the ideal Gaussian distribution of  $S(u'_\beta) = 0$  in the non-rotating pipe flow. However, as soon as the system rotation is imposed, this behaviour of  $S(u'_\beta)$  is broken, exhibiting a complex profile pattern in the radial direction.

[Figure 15\(b,d,f\)](#) compare the flatness factors of three velocity components at different rotation numbers. Apparently, all three flatness factors peak at the wall for both non-rotating and rotating pipe flows. As shown in [figure 15\(b\)](#), the profile of the axial flatness factor  $F(u'_z)$  has two zero-crossing points in the near-wall region of the pipe (such that it changes sign five times along a diameter). The two zero-crossing points are located at  $y = 0.033$  and  $y = 0.221$ , respectively, for the non-rotating flow. As the rotation number is increased, the profile of  $F(u'_z)$  deviates more apparently from the ideal Gaussian distribution showing an enhanced level of turbulence intermittency. Moreover, the two zero-crossing points tend to shift towards the pipe centre as the rotation number is increased. At the highest rotation number  $Ro_b = 20$ , the zero-crossing points are located at  $y = 0.399$  and at  $y = 0.667$ . From [figure 15\(d\)](#), it is seen that the value of  $F(u'_r)$  reaches its maximum at the wall at  $Ro_b = 2$ , which is almost threefold of that at  $Ro_b = 0$ . It is evident that the profile of  $F(u'_r)$  approaches the theoretical value of 3 of an ideal Gaussian distribution rapidly as the distance from the wall increases. As is evident from [figure 15\(f\)](#), the wall value of  $F(u'_\beta)$  is the highest in the non-rotating flow case ( $Ro_b = 0$ ), which drops rather rapidly as the rotation number is increased. At the two highest rotation numbers tested ( $Ro_b = 14$  and  $20$ ), the profile of  $F(u'_\beta)$  shows a complex pattern and deviates significantly from a Gaussian distribution at radial positions slightly off the pipe centre ( $0.5 < y < 0.9$ ).

In the analysis of the skewness factor associated with [figure 15](#), attention has been paid to the locations of its zero-crossing points. This is because of the sign of the skewness factor is critical in defining near-wall sweep and ejection events. In the context of a circular pipe flow, the ejection events feature  $S(u'_z) < 0$  and  $S(-u'_r) > 0$ , whereas the sweep events are characterised by  $S(u'_z) > 0$  and  $S(-u'_r) < 0$ . The ejection and sweep events correspond to the  $Q2$  (featuring  $u'_z < 0$  and  $-u'_r > 0$ ) and  $Q4$  (featuring  $u'_z > 0$  and  $-u'_r < 0$ ) events in the quadrant analysis of the radial-axial Reynolds shear stress, respectively.

[Figure 16](#) compares the ejection and sweep events of the non-rotating ( $Ro_b = 0$ ) and rotating ( $Ro_b = 20$ ) pipe flows based on the skewness factors of  $u'_z$  and  $-u'_r$ . The intervals corresponding to the ejection and sweep events are labelled in blue and red colours, respectively. These intervals are identified based on the zero-crossing points of  $S(u'_z)$  and  $S(-u'_r)$ . To ensure a clear view of the events, all profiles are plotted semi-logarithmically in the radial direction with respect to the wall coordinate  $y^+$ . For the non-rotating case shown in [figure 16\(a\)](#), the ejection events occur at  $y^+ \in [36.885, 180]$  (or,  $y \in [0.205, 1]$ ) in the log-law region, whereas the sweep events are observed at  $y^+ \in [4.101, 12.203]$  (or,  $y \in [0.023, 0.068]$ ) in the viscous sublayer. From [figure 16\(b\)](#), it is seen that as the rotation

DNS of turbulent pipe flow subjected to axial rotation

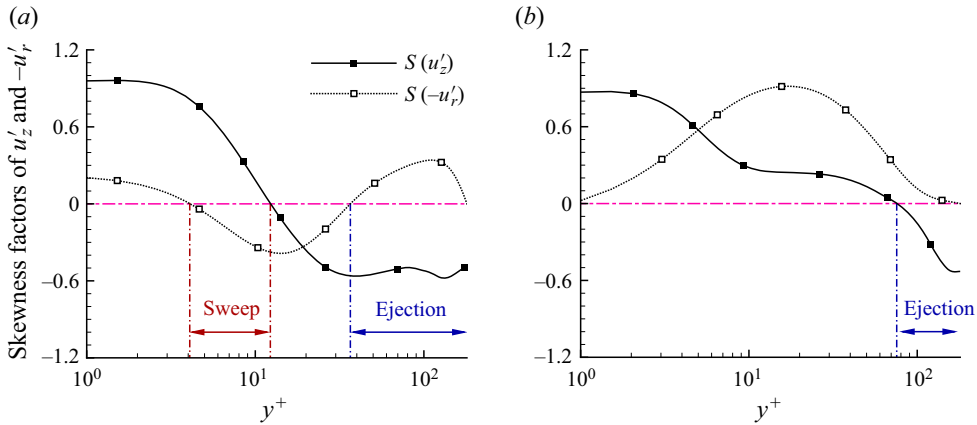


Figure 16. Profiles of skewness factors of  $u'_z$  and  $-u'_r$  of the (a) non-rotating ( $Ro_b = 0$ ) and (b) axially rotating ( $Ro_b = 20$ ) pipe flow cases. Pink horizontal dash-dotted line indicates the zero value of an ideal Gaussian distribution. The intervals corresponding to ejection and sweep events are labelled in blue and red colours, respectively. Results are based on test cases of the longest pipes at corresponding rotation numbers listed in table 1.

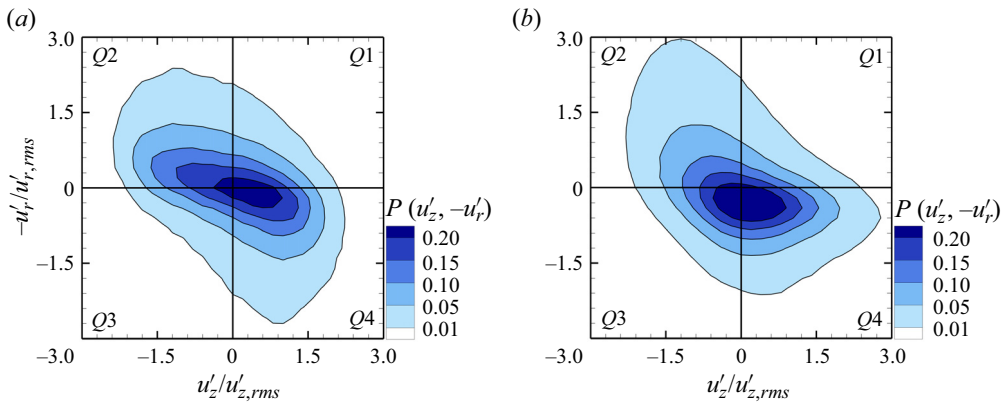


Figure 17. Contours of j.p.d.f.  $P(u'_z, -u'_r)$  at wall-normal position  $y^+ \approx 15$  of the pipe for the (a) non-rotating ( $Ro_b = 0$ ) and (b) axially rotating ( $Ro_b = 20$ ) pipe flows. All contours have been split into four quadrants (Q1–4) by black solid lines. Results are based on test cases of the longest pipes at corresponding rotation numbers listed in table 1.

number reaches  $Ro_b = 20$ , the ejection interval is shrunk by 27.30 % and shifts towards the pipe centre with  $y^+ \in [75.96, 180]$  (or,  $y \in [0.422, 1]$ ). In contrast to the non-rotating pipe flow, the disappearance of the sweep interval in the near-wall region of the pipe indicates that the axial system rotation impedes the formation of the near-wall turbulence structures by suppressing the sweep events. The analysis of sweep and ejection events is conducted solely based on the sign of the skewness factors,  $S(u'_z)$  and  $S(-u'_r)$ , which can only provide a partial explanation of the axially rotating effects on these two events. To refine the research, the joint probability density function (j.p.d.f.) can be further employed to perform a quadrant analysis of sweep and ejection events, and near-wall turbulence structures.

Figure 17 compares the contours of j.p.d.f. of  $u'_z$  and  $-u'_r$ , i.e.  $P(u'_z, -u'_r)$ , at the wall-normal position  $y^+ \approx 15$  of the pipe for the non-rotating ( $Ro_b = 0$ ) and rotating ( $Ro_b = 20$ ) pipe flows. This particular near-wall position is selected because the Reynolds

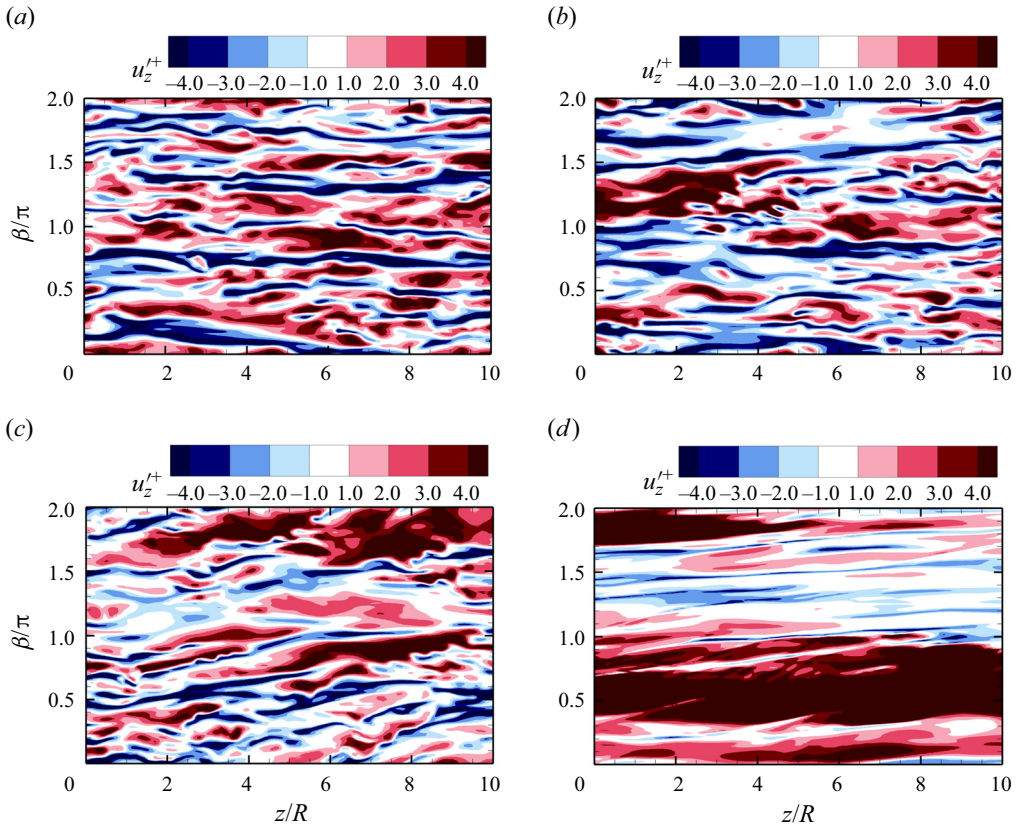


Figure 18. Contours of instantaneous axial velocity fluctuations ( $u_z'^+$ ) in the  $\beta$ - $z$  plane at wall-normal position  $y^+ \approx 15$  for the (a) non-rotating ( $Ro_b = 0$ ) and (b–d) axially rotating ( $Ro_b = 1, 2$  and  $20$ ) flows. The axial domain is arbitrarily extracted within range  $z/R \in [0, 10]$ . Results are based on test cases of the longest pipes at corresponding rotation numbers listed in [table 1](#).

stress component  $\langle u_z' u_z' \rangle^+$  reaches its maximum value at this radial position. From [figure 17\(a,b\)](#), it is evident that the  $Q2$  and  $Q4$  events are preferred, corresponding to the ejection and sweep events, respectively. However, as the rotation number is increased from  $Ro_b = 0$  to  $20$ , the  $Q2$  events tend to produce high intensities with a low probability, whereas the  $Q4$  events show an opposite trend.

### 3.6. Turbulent flow structures

[Figure 18](#) compares instantaneous axial turbulence structures (visualised using the contours of  $u_z'^+$ ) in the  $\beta$ - $z$  plane at the wall-normal position  $y^+ \approx 15$  for the non-rotating ( $Ro_b = 0$ ) and rotating ( $Ro_b = 1, 2$  and  $20$ ) pipe flows. The axial domain is arbitrarily selected within the range of  $z/R \in [0, 10]$ . At  $Ro_b = 0$  as shown in [figure 18\(a\)](#), the axial turbulence structures are purely streaks, visualised using contours of positively (indicated by red) and negatively valued (indicated by blue) instantaneous axial velocity fluctuations  $u_z'^+$ , which alternate in the azimuthal direction in the non-rotating pipe flow. At low rotation numbers  $Ro_b = 1$  and  $2$  shown in [figure 18\(b,c\)](#), it is interesting to see that the streaky structures in the near-wall region tilt slightly, a physical feature that relates to the secondary flows shown previously in [figure 3\(b\)](#). At  $Ro_b = 20$  as shown in [figure 18\(d\)](#), the

DNS of turbulent pipe flow subjected to axial rotation

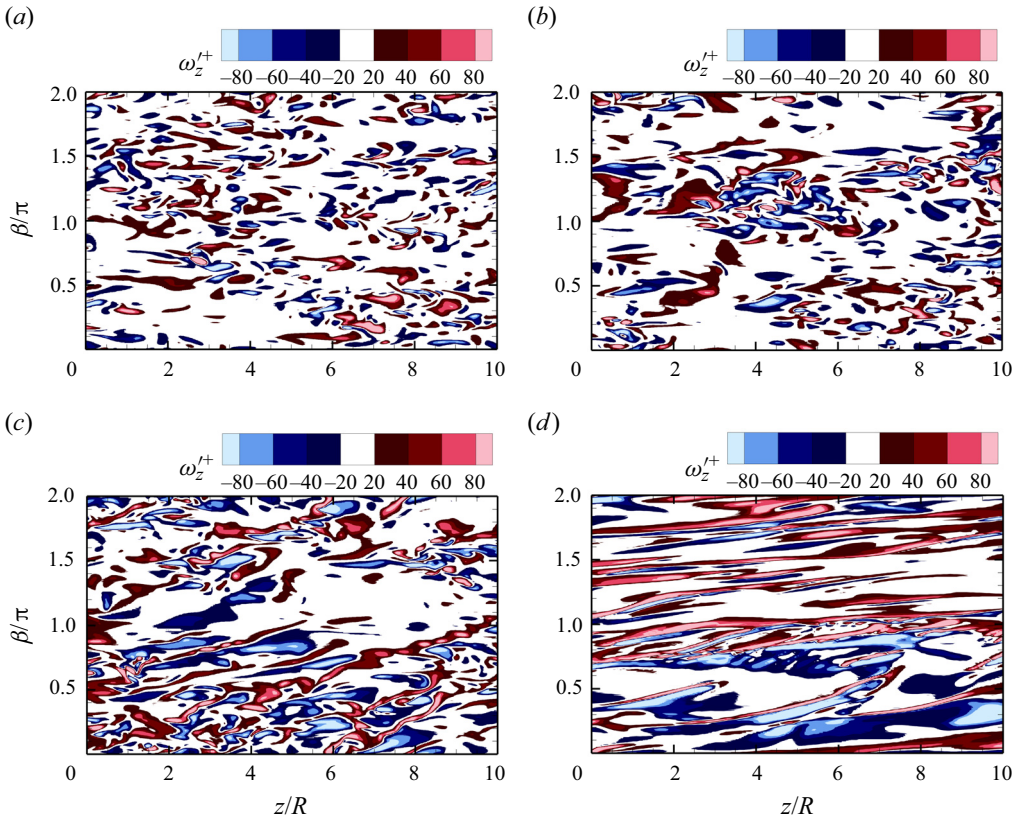


Figure 19. Contours of instantaneous axial vorticity fluctuations ( $\omega_z'^+$ ) in the  $\beta$ - $z$  plane at wall-normal position  $y^+ \approx 15$  for the (a) non-rotating ( $Ro_b = 0$ ) and (b-d) axially rotating ( $Ro_b = 1, 2$  and  $20$ ) pipe flows. The axial domain is arbitrarily extracted within range  $z/R \in [0, 10]$ . Results are based on test cases of the longest pipes at corresponding rotation numbers listed in [table 1](#).

patterns of axial turbulence structures are qualitatively different from those at zero or very low rotation numbers shown in [figure 18\(a-c\)](#) in the sense that they are now mixed with streaks and Taylor columns (at this high rotation number). Clearly, the axial turbulence structures are more intensified and their azimuthal period becomes greater at  $Ro_b = 20$ . From the previous discussion of [figure 10](#), it is further understood that peak magnitudes of  $II_{20}$  and  $III_{20}$  are larger than that of  $I_{20}$ , indicating that turbulence structures are dominated by Taylor columns (over the streaks) at the near-wall position of  $y^+ = 15$  at the highest rotation number tested ( $Ro_b = 20$ ).

[Figure 19](#) compares instantaneous axial vorticity fluctuation ( $\omega_z'^+$ ) patterns in the  $\beta$ - $z$  plane at  $y^+ \approx 15$  for the non-rotating ( $Ro_b = 0$ ) and rotating ( $Ro_b = 1, 2$  and  $20$ ) pipe flows. For the non-rotating pipe flow shown in [figure 19\(a\)](#), numerous near-wall small-scale vortical structures are seen in the  $\beta$ - $z$  plane. However, in response to the axial system rotation, these small-scale structures tend to stretch along the axial direction and tilt slightly along the azimuthal direction at  $Ro_b = 1$  and  $2$ , a pattern that is consistent with the observation of [figure 18\(b,c\)](#). At the highest rotation number  $Ro_b = 20$  as shown [figure 19\(d\)](#), the vortical structures become greatly stretched in the axial direction. The instantaneous vortical structures at zero or very low rotation numbers ( $Ro_b = 0-2$ ) mainly reflect the characteristics of the turbulent boundary layer of a viscous flow. However, at



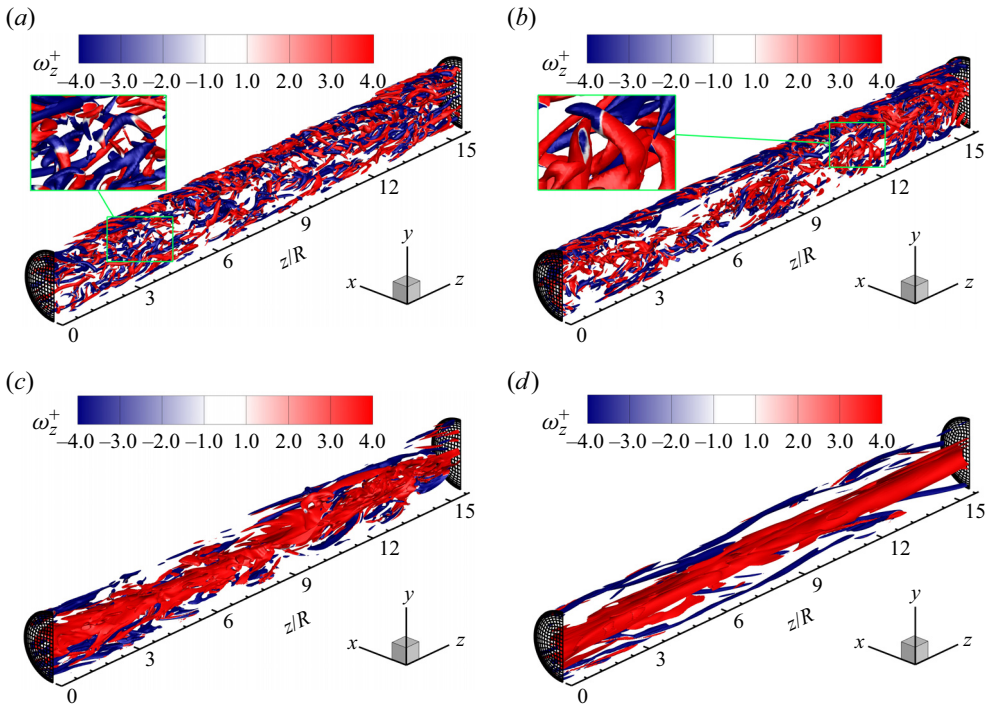


Figure 20. Contours of vortical structures of the (a) non-rotating ( $Ro_b = 0$ ) and (b–d) axially rotating ( $Ro_b = 2, 6$  and  $14$ ) flows. For clarity, only one half of the azimuthal domain is displayed. The axial domain (iso-surfaces are plotted with  $\lambda_{ci} = 1.1$ ) is arbitrarily extracted within range  $z/R \in [0, 15]$ . All contours are coloured by non-dimensionalised instantaneous axial vorticity  $\omega_z^+$ . The blue (representing negatively valued  $\omega_z^+$ ) and red (representing positively valued  $\omega_z^+$ ) flow structures correspond to the clockwise and counterclockwise spiral motions, respectively. Results are based on test cases of the longest pipes at corresponding rotation numbers listed in table 1.

the highest rotation number  $Ro_b = 20$ , Taylor columns become dominant, a mechanism that is described by the Taylor–Proudman theorem of the inviscid flow theory and is fundamentally different from that of a boundary layer.

Figure 20 compares the coherent structures of the non-rotating ( $Ro_b = 0$ ) and rotating ( $Ro_b = 2, 6$  and  $14$ ) pipe flows. To visualise the coherent structures, the swirling strength ( $\lambda_{ci}$ ) criterion of Zhou *et al.* (1999) is used, which is defined as the imaginary part of the complex eigenvalue of the velocity gradient tensor. The iso-surfaces of the flow structures are further coloured by non-dimensionalised instantaneous axial vorticity  $\omega_z^+$ . Therefore, the blue (representing negatively valued  $\omega_z^+$ ) and red (representing positively valued  $\omega_z^+$ ) flow structures correspond to the clockwise and counterclockwise spiral motions with respect to the axial direction, respectively. Furthermore, in order to provide a clear view of the hairpin structures at zero or low rotation numbers and Taylor columns at high rotation numbers (see also figure 3), only one half of the azimuthal domain is displayed, arbitrarily extracted within the axial range of  $z/R \in [0, 15]$ . In figure 20(a), the hairpin structures are clearly observed in the non-rotating pipe flow, which are qualitatively similar to those reported in Wu *et al.* (2015). In the literature, the discussion of hairpin structures is often made based on turbulent boundary-layer flows developing over flat plates, and the formation of a standard complete hairpin structure model of a ‘head–neck–legs’ pattern is often attributed to near-wall bursting events, spreading to the outer region through the



$Q2$  and  $Q4$  events (Robinson 1991; Adrian 2007). The presence of hairpin structures is also evident at  $Ro_b = 2$  shown in figure 20(b). It is seen that in response to the system rotation imposed (at  $Ro_b = 2$ ), a number of counterclockwise vortical structures (aligned in the  $z$ -direction, corresponding to positively valued  $\omega_z^+$ ) begin to become populated at the pipe centre, whereas some clockwise vortical structures (corresponding to negatively valued  $\omega_z^+$ ) are shifted away from the pipe centre. Because of the low axial system rotating speed at  $Ro_b = 2$ , the secondary flows are not strong enough to result in any significant migration of the flow structures. However, as the rotation number continues to increase to  $Ro_b = 6$  and 14, such spatial evolution of the flow structures becomes apparent. The effects of rotation number on the instantaneous flow structures observed here are consistent with the profile trend of the mean axial vorticity  $\langle \omega_z \rangle^+$  demonstrated previously in figure 5(c), which clearly shows that as  $Ro_b$  increases, the value of  $\langle \omega_z \rangle^+$  becomes increasingly negative (corresponding to local clockwise rotation) in the near-wall region (for  $0 \leq y < 0.4$ ) and positive (corresponding to local counterclockwise rotation) in the pipe centre (for  $0.4 < y \leq 1.0$ ).

From figure 20(c), it is seen that as the rotation number is increased to  $Ro_b = 6$ , stabler and stronger large-scale secondary motion occurs at the pipe centre, as a result of the occurrence of Taylor columns. Meanwhile, hairpin structures are considerably destructed by the axial system rotation. As the rotation number further increases to  $Ro_b = 14$  as shown in figure 20(d), it is seen that the vortical flow structures corresponding to positively and negatively valued  $\omega_z^+$  become visibly separated as most of the structures of positively valued  $\omega_z^+$  cluster together at the pipe centre to form very long secondary vortical structures of Taylor columns which spin counterclockwise (see also figure 3).

#### 4. Conclusions

Turbulent flow confined within a circular pipe subjected to axial system rotation has been studied using DNS for a wide range of rotation numbers varying from  $Ro_b = 0$  to 20. To ensure that energetic turbulent eddy motions in form of hairpins and Taylor columns are reasonably captured at different rotation numbers, pipes of length up to  $L_z = 180\pi R$  are used in DNS.

The bulk mean velocity  $U_b^+$  increases as soon as the axial system rotation is imposed, and reaches its maximum at  $Ro_b = 2$ . However, at higher rotation numbers for  $Ro_b \geq 6$ , the value of  $U_b^+$  decreases significantly. It is interesting to observe that the peak position of the mean swirl (azimuthal) velocity  $r\langle u_\beta \rangle^+/R$  is independent of  $Ro_b$ , which occurs at  $y \approx 0.4$  where the mean axial vorticity  $\langle \omega_z \rangle^+$  is zero identically. For a non-rotating pipe flow,  $\langle u'_r u'_\beta \rangle^+ \equiv 0$  and  $\langle u'_\beta u'_z \rangle^+ \equiv 0$ . By contrast, in response to the axial system rotation imposed, all six Reynolds stress components are non-trivial. Under an axial system rotation, secondary flows are induced, which tend to suppress  $\langle u'_z u'_z \rangle^+$  in the near-wall region but enhance the magnitudes of  $\langle u'_r u'_r \rangle^+$  and  $\langle u'_\beta u'_\beta \rangle^+$  in most pipe regions. This leads to a significant increase in the TKE level as the rotation number is increased. However, as the rotation number further increases from  $Ro_b = 14$  to 20, the TKE value becomes stable. In the context of an axially rotating pipe flow, the total shear stress  $\tau_{rz}^{tot+}$  in the  $r$ - $z$  plane exhibits a linear profile in the radial direction. By contrast, it is proven that the total shear stress  $\tau_{r\beta}^{tot+}$  in the  $r$ - $\beta$  plane is zero identically such that the profiles of  $\tau_{r\beta}^{vis}$  and  $-\langle u'_r u'_\beta \rangle^+$  are mirror reflections of each other.

As the rotation number is increased, the profile of flatness factor  $F(u'_z)$  deviates apparently from the ideal Gaussian distribution showing an enhanced level of turbulence intermittency. It is observed that the azimuthal skewness factor generally follows the ideal

Gaussian distribution of  $S(u'_\beta) = 0$  in the non-rotating pipe flow. However, as soon as the system rotation is imposed, this behaviour of  $S(u'_\beta)$  is broken, exhibiting a complex profile pattern in the radial direction. Furthermore, based on the analysis of the signs of  $S(u'_z)$  and  $S(-u'_r)$ , it is observed that the axial system rotation tends to impede the formation of hairpin structures by suppressing the sweep events.

There are two types of energetic axial flow structures in an axially rotating pipe flow. The first type is hairpin structures (associated with streaks in the near-wall region), typical of a turbulent boundary layer over a solid wall. The second type is the Taylor columns, which spin in the azimuthal direction and elongate in the axial direction at moderate and high rotation numbers. The streaks and Taylor columns are distinctively different in terms of their characteristic wavelengths corresponding to the peaks (*I* for hairpin and streaks, and peaks *II* and *III* for Taylor columns) of the premultiplied spectra  $k_z \tilde{E}_{ii}$ . It is interesting to observe that Taylor columns feature one single dominant peak *II* at moderate rotation numbers, but two dominant peaks *II* and *III* at high rotation numbers. It is also observed that as the rotation number is increased, Taylor columns become increasingly populated in the central regions of the pipe, and furthermore, turbulence kinetic energy held by Taylor columns enhances rapidly associated with significant increases in their axial length scales. As such, both the magnitude and characteristic wavelength of peak *III* increases drastically as the rotation number is increased. In view of this, a rather long pipe is needed for performing DNS of an axially rotating pipe flow at high rotation numbers in order to capture Taylor columns. Through a complementary comparative study of test cases of different pipe lengths, it is observed that use of short pipes can lead to physically inaccurate flow statistics and velocity spectra at high rotation numbers.

Although a very long pipe of  $L_z = 180\pi R$  has been used for conducting DNS at the highest rotation number  $Ro_b = 20$  in this study, a longer pipe would be needed if a higher rotation number was further pursued. It is also recognised that our comparative study of eight rotation numbers has been conducted based on a fixed low Reynolds number. The combined effects of both Reynolds and rotation numbers on axially rotating turbulent pipe flow and structures are still unknown, which need to be explored in future studies.

**Acknowledgement.** The authors would like to thank Blackburn & Sherwin (2004) for making their spectral-element code ‘Semtex’ accessible to the research community.

**Funding.** The Digital Research Alliance of Canada is acknowledged for providing us with access to supercomputing and storage facilities. Research funding from Natural Sciences and Engineering Research Council (NSERC) of Canada to B.-C.W. (Grant No. RGPIN-2019-06735) is gratefully acknowledged.

**Declaration of interests.** The authors report no conflict of interest.

**Author ORCIDs.**

① Zhao-Ping Zhang <https://orcid.org/0009-0001-5745-931X>;

① Bing-Chen Wang <https://orcid.org/0000-0003-0883-4897>.

## Appendix A. Effects of pipe length on the accuracy of DNS results

A turbulence field consists of eddies of different temporal and spatial scales. Thus, in a high-fidelity numerical or experimental study of a transient turbulent flow problem, the frequency and wavelength ranges of energetic eddy motions need to be carefully considered. Since the pioneering work of Jiménez & Moin (1991), it has become understood that a minimum computational domain is needed in DNS in order to capture major physical processes associated with large energetic turbulence structures such as near-wall hairpins and streaks in a plane-channel flow. In the context of an axially rotating

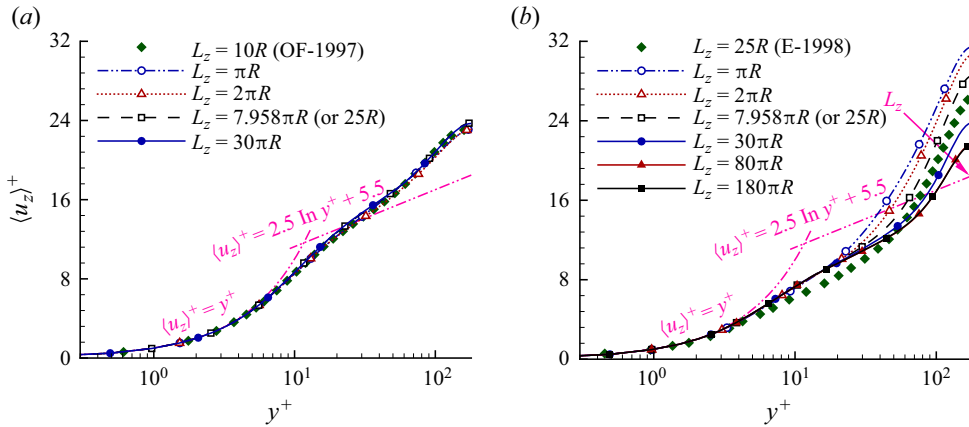


Figure 21. Profiles of the mean axial velocity  $\langle u_z \rangle^+$  computed based on varying pipe lengths  $L_z$  at two rotation numbers (a)  $Ro_b = 2$  and (b)  $Ro_b = 20$ , based on test cases listed in table 2. For the purpose of comparison, the DNS results of Orlandi & Fatica (1997, labelled as ‘OF-1997’) and Ebstein (1998, labelled as ‘E-1998’) are displayed. The pink arrow points in the direction of increasing pipe length.

turbulent pipe flow, the axial turbulent motions are dominated by streaks at low rotation numbers, and by Taylor columns at moderate and high rotation numbers. Because the characteristic length scales of both streaks and Taylor columns increase as the rotation number  $Ro_b$  is increased, the pipe length  $L_z$  needs to be increased accordingly in DNS. Previous studies of the domain size effects on the accuracy of the DNS results have focused primarily on boundary-layer flows over flat plates. In this appendix, we study the effects of pipe length on the accuracy of DNS results in the context of an axially rotating pipe flow. A comparative study of 10 DNS cases of varying pipe lengths has been conducted at low and high rotation numbers ( $Ro_b = 2$  and 20). The pipe lengths, Reynolds numbers and grid resolutions of the 10 DNS test cases are summarised in table 2, in which the pipe length varies drastically from  $L_z = \pi R$  to  $180\pi R$ .

### A.1. Impact on the mean velocity

Figure 21 compares the mean axial velocity  $\langle u_z \rangle^+$  computed based on a variety of pipe lengths at two rotation numbers  $Ro_b = 2$  and 20. For the purpose of comparison, the DNS data of Orlandi & Fatica (1997, based on a pipe length of  $L_z = 10R$  (or  $3.183\pi R$ )) and Ebstein (1998, based on a pipe length of  $L_z = 25R$  (or  $7.958\pi R$ )) at a similar Reynolds number of  $Re_b = 4900$  are also displayed in the figures. In addition, the classical law of the wall for a non-rotating turbulent circular pipe flow based on von Kármán’s two-layer boundary-layer model (i.e.  $\langle u_z \rangle^+ = y^+$  for  $y^+ \leq 10.8$  and  $\langle u_z \rangle^+ = 2.5 \ln y^+ + 5.5$  for  $y^+ > 10.8$ ) is shown to highlight the influence of axial system rotation on the mean axial velocity profile. By comparing figures 21(a) and 21(b), it is clear that the values of  $\langle u_z \rangle^+$  of test cases of different pipe lengths agree better at the lower rotation number  $Ro_b = 2$  than at the higher rotation number  $Ro_b = 20$ . In other words, the effect of pipe length on the prediction of  $\langle u_z \rangle^+$  manifests as the rotation number is increased. At the highest rotation number shown in figure 21(b), it is clear that the profiles of  $\langle u_z \rangle^+$  of all seven cases become increasingly different in values as the pipe centre is approached. The results from the short pipes (of  $L_z = \pi R$ – $7.958\pi R$ ) based on either our simulations or those of Ebstein (1998) all deviate considerably from those of longer pipes (of  $L_z = 30\pi R$ – $180\pi R$ ). The pipe length

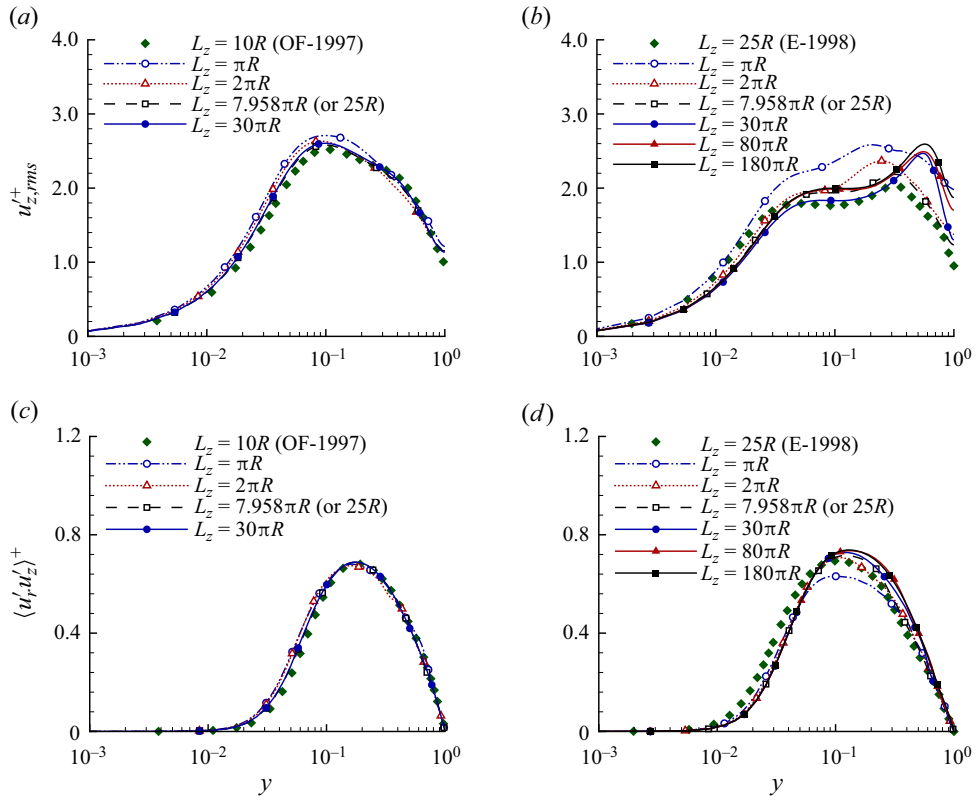


Figure 22. Profiles of non-dimensionalised (a,b) axial turbulence intensity  $u_{z,rms}^+$  and (c,d) Reynolds shear stress  $\langle u_r' u_z' \rangle^+$  for different pipe lengths ( $L_z$ ) at two rotation numbers (a,c)  $Ro_b = 2$  and (b,d)  $Ro_b = 20$  (based on the test cases of table 2). The DNS results of Orlandi & Fatica (1997, labelled as ‘OF-1997’) and Ebstein (1998, labelled as ‘E-1998’) are displayed for the purpose of comparison.

effect is evident in terms of the calculation of the mean axial velocity  $\langle u_z \rangle^+$ , and will be further demonstrated based on the calculations of root-mean-square (r.m.s.) velocities, Reynolds shear stresses, two-point autocorrelation coefficients and premultiplied spectra of velocity fluctuations.

### A.2. Impact on the second-order statistical moments

Figure 22 compares the profiles of the second-order statistical moments of  $Ro_b = 2$  and 20 obtained based on test cases of varying pipe lengths described in table 2. For the purpose of comparison, the DNS data of Orlandi & Fatica (1997) and Ebstein (1998) are also displayed in the figure. The second-order statistical moments of the velocity field are non-dimensionalised using the mean axial velocity at the pipe centreline  $\langle U_{CL} \rangle$  in Orlandi & Fatica (1997) and are presented in a dimensional form in Orlandi & Ebstein (2000). The Reynolds stresses and r.m.s. velocities non-dimensionalised using the wall friction velocity  $u_\tau$  are available in Ebstein (1998).

From figure 22(a,c), it is clear that predictions of  $u_{z,rms}^+$  and  $\langle u_r' u_z' \rangle^+$  based on cases of different pipe lengths are generally similar at the lower rotation number  $Ro_b = 2$ , although the value of  $u_{z,rms}^+$  obtained using the shortest pipe length ( $L_z = \pi R$ ) is slightly over-predicted in comparison with those obtained using longer pipes. However, as the

DNS of turbulent pipe flow subjected to axial rotation

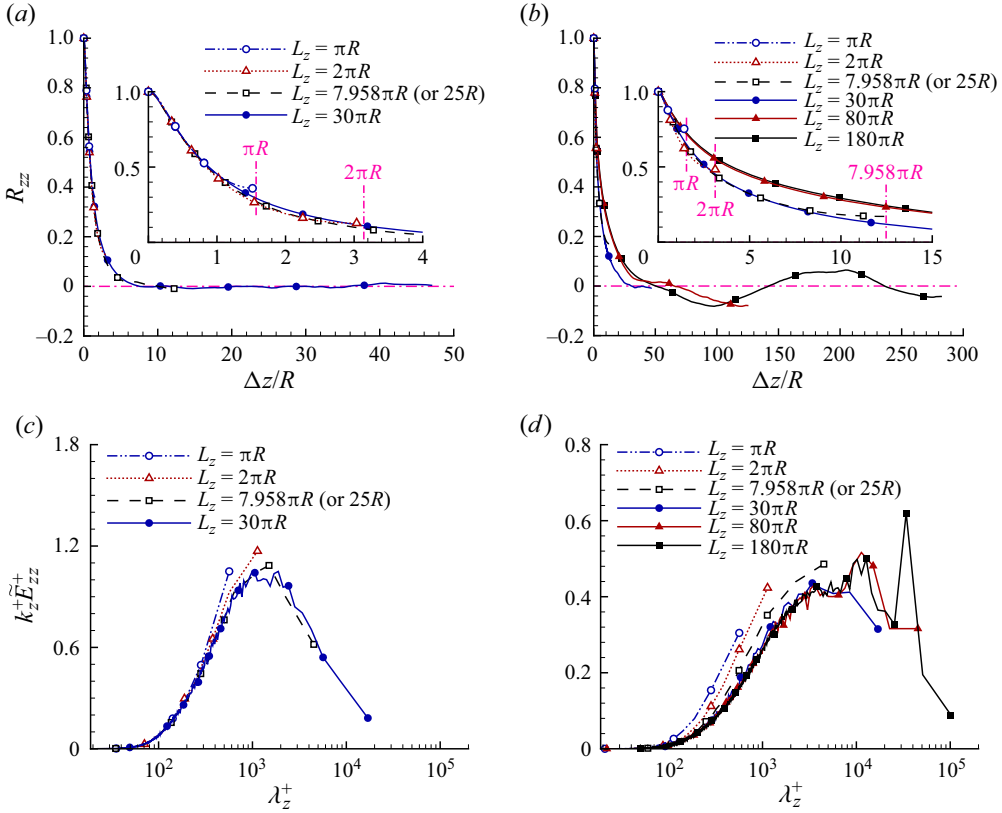


Figure 23. Influence of pipe length on the predictive accuracy of DNS with respect to the (a,b) axial two-point autocorrelation coefficient  $R_{zz}$  and (c,d) premultiplied axial velocity spectra  $k_z^+ \tilde{E}_{zz}^+$  at two rotation numbers (a,c)  $Ro_b = 2$  and (b,d)  $Ro_b = 20$ , based on test cases of different pipe lengths listed in table 2. The values of  $R_{zz}$  and  $k_z^+ \tilde{E}_{zz}^+$  are calculated along the streamwise direction at wall-normal position  $y = 0.083$  (or  $y^+ \approx 15$ ).

rotation number is increased to  $Ro_b = 20$ , it shows clearly in figure 22(b,d) that the DNS results of both  $u'_{z,rms}^+$  and  $\langle u'_r u'_z \rangle^+$  based on the three shortest pipe lengths (of  $L_z = \pi R - 7.958R$ ) of either our current study or those of Ebstein (1998) deviate from those of longer pipes (of  $L_z = 30\pi R - 180\pi R$ ). From figure 22(b,d), it is seen that the performance of the shortest-pipe-length case of  $L_z = \pi R$  is the least satisfactory. Furthermore, the impact of pipe length on the calculation of the second-order statistical moments is the most apparent with respect to the profiles of  $u'_{z,rms}^+$  at  $Ro_b = 20$  shown in figure 22(b). Clearly, in order to calculate the values of  $u'_{z,rms}^+$  and  $\langle u'_r u'_z \rangle^+$  accurately at the highest rotation number  $Ro_b = 20$ , the minimum pipe length needs to be kept at  $L_z = 30\pi R$ .

A.3. Impact on the two-point correlations and energy spectra

The pipe length effects on the predictive accuracy of DNS with respect to the value of the axial two-point correlation  $R_{zz}$  and that of the non-dimensionalised premultiplied 1-D spectrum of axial velocity fluctuations  $k_z^+ \tilde{E}_{zz}^+$  are demonstrated in figure 23. As indicated by table 2, the largest pipe length is  $L_z = 30\pi R$  and  $180\pi R$  at  $Ro_b = 2$  and 20, respectively, which ensure the value of  $R_{zz}$  approaches zero and that of  $k_z^+ \tilde{E}_{zz}^+$  is sufficiently low at the cutoff wavelength. From figure 23(a,b), it is clear that the profile  $R_{zz}$  truncates at

a high level if short pipes are used for  $L_z \leq 2\pi R$  (at  $Ro_b = 2$ ) and for  $L_z \leq 7.958\pi R$  (at  $Ro_b = 20$ ). In these short-pipe-length cases, the value of  $R_{zz}$  is considerably above zero and, therefore, they are incapable of capturing the signature point of the maximum negative correlation that corresponds to the characteristic length scale of the energetic flow structures. A similar situation holds in the profiles of  $k_z^+ \tilde{E}_{zz}^+$  shown in figure 23(c,d). From figure 23(c), it is seen that the two short-pipe-length cases of  $L_z \leq 2\pi R$  are unable to capture the full dome peak (i.e. peak  $I_2$ ) of  $k_z^+ \tilde{E}_{zz}^+$  at  $Ro_b = 2$ . At the high rotation number of  $Ro_b = 20$ , the two short-pipe-length cases of  $L_z \leq 2\pi R$  completely miss the prediction of all three peaks (i.e. peak  $I_{20}$ ,  $II_{20}$  and  $III_{20}$ ) of  $k_z^+ \tilde{E}_{zz}^+$ . Although the case of  $L_z = 30\pi R$  is able to capture peak  $I_{20}$ , it misses peaks  $II_{20}$  and  $III_{20}$  in its prediction. Even in the case of a larger pipe length  $L_z = 80\pi R$ , peak  $III_{20}$  is still missed in the DNS prediction. Therefore, in order to capture the energetic eddy motions of Taylor columns (as indicated by its two signature modal wavelengths of peaks  $II_{20}$  and  $III_{20}$ ), the pipe length needs to be kept at  $L_z = 180\pi R$  (which has a relatively small premultiplied energy spectrum loss that is 14.32 % of its peak value at its cutoff wavelength).

#### A.4. Impact on the ratio of axial integral scale over pipe length

From the comparative study based on cases of different pipe lengths of table 2, it is clear that an overly short pipe can give spurious calculations of the first- and second-order flow statistics, and the values of the axial two-point correlation  $R_{zz}$  and premultiplied spectrum of axial velocity fluctuations  $k_z^+ \tilde{E}_{zz}^+$  in DNS. To further demonstrate, the values of the zero mode of  $k_z^+ \tilde{E}_{zz}^+$  calculated based on test cases of different pipe lengths can be compared. At a fixed radial position  $r$ ,  $\tilde{E}_{zz}(r, k_z)$  varies with  $k_z$  only and, therefore, can be denoted using  $\tilde{E}_{zz}(k_z)$  for simplicity. At the zero mode ( $k_z = 0$ ), the axial velocity spectrum relates to the axial Reynolds normal stress as

$$\tilde{E}_{zz}(0) = \frac{l_{int,z}}{L_z} \langle u'_z u'_z \rangle, \tag{A1}$$

where  $l_{int,z} = \int_0^{L_z} R_{zz} dz$  is the integral length scale of the axial ( $z$ ) direction. We can rearrange this equation to obtain

$$\frac{\tilde{E}_{zz}(0)}{\langle u'_z u'_z \rangle} = \frac{l_{int,z}}{L_z}, \tag{A2}$$

which has clear physical meaning that at the zero mode, the axial velocity spectra  $\tilde{E}_{zz}(0)$  non-dimensionalised by  $\langle u'_z u'_z \rangle$  is the ratio of the axial integral length  $l_{int,z}$  over the pipe length  $L_z$ . The value of  $l_{int,z}/L_z$  would approach zero, if the pipe length is significantly larger than the axial integral length scale. Figure 24 shows the value of  $l_{int,z}/L_z$  computed based on test cases of varying pipe lengths listed in table 2. From figure 24, it is clear that the axial integral length is much larger at  $Ro_b = 20$  than at  $Ro_b = 2$ . This is expected, because both streaky structures and Taylor columns become increasingly elongated as the rotation number is increased. The percentage value of  $l_{int,z}/L_z$  is 59.3 % and 36.9 % for the shortest pipe lengths of  $L_z = \pi R$  and  $2\pi R$  at  $Ro_b = 2$ . Both these percentage values are too large to be acceptable in DNS, because they indicate that the axial integral length scale are of the same order of the pipe length (as such, there is insufficient room for large turbulence structures to move and develop axially). At the high rotation number  $Ro_b = 20$ , the percentage value of  $l_{int,z}/L_z$  is as high as 83.7 % in the shortest-pipe-length case of



## DNS of turbulent pipe flow subjected to axial rotation

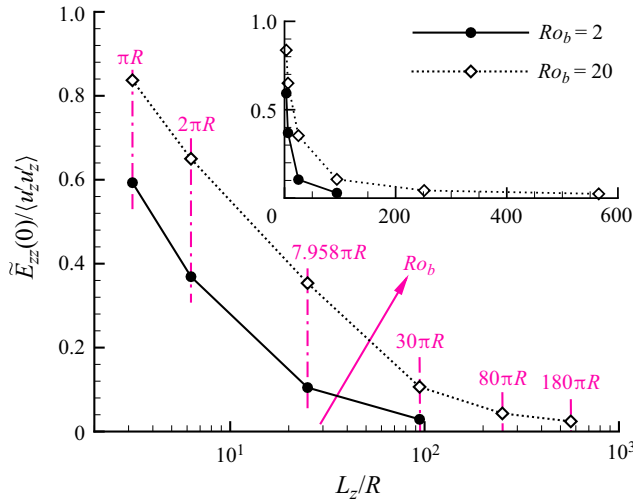


Figure 24. Influence of the pipe length on DNS prediction of the axial velocity spectra  $\tilde{E}_{zz}$  (non-dimensionalised by  $\langle u'_z u'_z \rangle$ ) at zero mode ( $k_z = 0$ ) with respect to axial pipe length  $L_z/R$  at two rotation numbers  $Ro_b = 2$  and 20, calculated along the streamwise direction at wall-normal position  $y = 0.083$  (or  $y^+ \approx 15$ ). The calculations are based on test cases listed in table 2. Pink arrow points to the direction of an increasing rotation number.

$L_z = \pi R$ , a scenario that is also physically unacceptable for DNS. By contrast, in the two longest-pipe cases of  $L_z = 80\pi R$  and  $180\pi R$  for  $Ro_b = 20$ , the percentage value of  $l_{int,z}/L_z$  drops to 4.3% and 2.4%, respectively, indicating the pipes are sufficiently long to allow large eddy motions (of integral length scales) to develop spatially.

### REFERENCES

- ADRIAN, R.J. 2007 Hairpin vortex organization in wall turbulence. *Phys. Fluids* **19** (4), 041301.
- AVSARKISOV, V., HOYAS, S., OBERLACK, M. & GARCÍA-GALACHE, J.P. 2014 Turbulent plane Couette flow at moderately high Reynolds number. *J. Fluid Mech.* **751**, R1.
- BAGHERI, E., WANG, B.-C. & YANG, Z. 2020 Influence of domain size on direct numerical simulation of turbulent flow in a moderately curved concentric annular pipe. *Phys. Fluids* **32** (6), 065105.
- BALTZER, J.R., ADRIAN, R.J. & WU, X. 2013 Structural organization of large and very large scales in turbulent pipe flow simulation. *J. Fluid Mech.* **720**, 236–279.
- BARTELLO, P., MÉTAIS, O. & LESIEUR, M. 1994 Coherent structures in rotating three-dimensional turbulence. *J. Fluid Mech.* **273**, 1–29.
- BLACKBURN, H.M. & SHERWIN, S.J. 2004 Formulation of a Galerkin spectral element – Fourier method for three-dimensional incompressible flows in cylindrical geometries. *J. Comput. Phys.* **197**, 759–778.
- BUZZICOTTI, M., ALUIE, H., BIFERALE, L. & LINKMANN, M. 2018 Energy transfer in turbulence under rotation. *Phys. Rev. Fluids* **3**, 034802.
- CHIN, C., OOI, A.S.H., MARUSIC, I. & BLACKBURN, H.M. 2010 The influence of pipe length on turbulence statistics computed from direct numerical simulation data. *Phys. Fluids* **22** (11), 115107.
- EBSTEIN, D. 1998 Reynolds Stresses and Kinetic Energy Budgets in the Flow through an Axially Rotating Pipe, PhD thesis, Sapienza University of Rome, Italy.
- EGGELS, J.G.M., UNGER, F., WEISS, M.H., WESTERWEEL, J., ADRIAN, R.J., FRIEDRICH, R. & NIEUWSTADT, F.T.M. 1994 Fully developed turbulent pipe flow: a comparison between direct numerical simulation and experiment. *J. Fluid Mech.* **268**, 175–210.
- FACCILOLO, L., TILLMARK, N., TALAMELLI, A. & ALFREDSSON, P.H. 2007 A study of swirling turbulent pipe and jet flows. *Phys. Fluids* **19**, 035105.
- FANG, X.-J. & WANG, B.-C. 2018 On the turbulent heat transfer in a square duct subjected to spanwise system rotation. *Intl J. Heat Fluid Flow* **71**, 220–230.

- FANG, X.-J., YANG, Z.-X., WANG, B.-C. & BERGSTROM, D.J. 2017 Direct numerical simulation of turbulent flow in a spanwise rotating square duct at high rotation numbers. *Intl J. Heat Fluid Flow* **63**, 88–98.
- FEIZ, A.A., OULD-ROUIS, M. & LAURIAT, G. 2003 Large eddy simulation of turbulent flow in a rotating pipe. *Intl J. Heat Fluid Flow* **24** (3), 412–420.
- GALLET, B. 2015 Exact two-dimensionalization of rapidly rotating large-Reynolds-number flows. *J. Fluid Mech.* **783**, 412–447.
- GRUNDESTAM, O., WALLIN, S. & JOHANSSON, A.V. 2008 Direct numerical simulations of rotating turbulent channel flow. *J. Fluid Mech.* **598**, 177–199.
- HIRAI, S., TAKAGI, T. & MATSUMOTO, M. 1988 Predictions of the laminarization phenomena in an axially rotating pipe flow. *Trans. ASME J. Fluids Engng* **110** (4), 424–430.
- HOYAS, S. & JIMÉNEZ, J. 2006 Scaling of the velocity fluctuations in turbulent channels up to  $Re_\tau = 2003$ . *Phys. Fluids* **18**, 011702.
- IMAO, S., ITOH, M. & HARADA, T. 1996 Turbulent characteristics of the flow in an axially rotating pipe. *Intl J. Heat Fluid Flow* **17**, 444–451.
- JAKIRLIĆ, S., HANJALIĆ, K. & TROPEA, C. 2002 Modeling rotating and swirling turbulent flows: a perpetual challenge. *AIAA J.* **40** (10), 1984–1996.
- JIMÉNEZ, J. & MOIN, P. 1991 The minimal flow unit in near-wall turbulence. *J. Fluid Mech.* **225**, 213–240.
- VAN KAN, A. & ALEXAKIS, A. 2020 Critical transition in fast-rotating turbulence within highly elongated domains. *J. Fluid Mech.* **899**, A33.
- KARNIADAKIS, G.E., ISRAELI, M. & ORSZAG, S.A. 1991 High-order splitting methods for the incompressible Navier–Stokes equations. *J. Comput. Phys.* **97** (2), 414–443.
- KARNIADAKIS, G.E. & SHERWIN, S.J. 2005 *Spectral/hp Element Methods for Computational Fluid Dynamics*, 2nd edn. Oxford University Press.
- KIKUYAMA, K., MURAKAMI, M. & NISHIBORI, K. 1983a Development of three-dimensional turbulent boundary layer in an axially rotating pipe. *Trans. ASME J. Fluids Engng* **105** (2), 154–160.
- KIKUYAMA, K., MURAKAMI, M., NISHIBORI, K. & MAEDA, K. 1983b Flow in an axially rotating pipe: a calculation of flow in the saturated region. *Bull. JSME* **26** (214), 506–513.
- KRISTOFFERSEN, R. & ANDERSSON, H.I. 1993 Direct simulations of low-Reynolds-number turbulent flow in a rotating channel. *J. Fluid Mech.* **256**, 163–197.
- MURAKAMI, M. & KIKUYAMA, K. 1980 Turbulent flow in axially rotating pipes. *Trans. ASME J. Fluids Engng* **102** (1), 97–103.
- OBERLACK, M. 1999 Similarity in non-rotating and rotating turbulent pipe flows. *J. Fluid Mech.* **379**, 1–22.
- OBERLACK, M., CABOT, W., PETERSSON REIF, B.A. & WELLER, T. 2006 Group analysis, direct numerical simulation and modelling of a turbulent channel flow with streamwise rotation. *J. Fluid Mech.* **562**, 383–403.
- ORLANDI, P. 1997 Helicity fluctuations and turbulent energy production in rotating and non-rotating pipes. *Phys. Fluids* **9** (7), 2045–2056.
- ORLANDI, P. & EBSTEIN, D. 2000 Turbulent budgets in rotating pipes by DNS. *Intl J. Heat Fluid Flow* **21** (5), 499–505.
- ORLANDI, P. & FATICA, M. 1997 Direct simulations of turbulent flow in a pipe rotating about its axis. *J. Fluid Mech.* **343**, 43–72.
- PALLARES, J. & DAVIDSON, L. 2000 Large-eddy simulations of turbulent flow in a rotating square duct. *Phys. Fluids* **12** (11), 2878–2894.
- PESTANA, T. & HICKEL, S. 2020 Rossby-number effects on columnar formation and the energy dissipation law in homogeneous rotating turbulence. *J. Fluid Mech.* **885**, A7.
- RECKTENWALD, I., ALKISHRIWI, N. & SCHRÖDER, W. 2009 PIV-LES analysis of channel flow rotating about the streamwise axis. *Eur. J. Mech. (B/Fluids)* **28** (5), 677–688.
- RECKTENWALD, I., WELLER, T., SCHRÖDER, W. & OBERLACK, M. 2007 Comparison of direct numerical simulations and particle-image velocimetry data of turbulent channel flow rotating about the streamwise axis. *Phys. Fluids* **19** (8), 085114.
- REICH, G. & BEER, H. 1989 Fluid flow and heat transfer in an axially rotating pipe. I. Effect of rotation on turbulent pipe flow. *Intl J. Heat Mass Transfer* **32** (3), 551–562.
- ROBINSON, S.K. 1991 Coherent motions in the turbulent boundary layer. *Annu. Rev. Fluid Mech.* **23** (1), 601–639.
- ROSAS, R.H. & WANG, B.C. 2022 DNS study of turbulent heat transfer in an elliptical pipe flow subjected to system rotation about the major axis. *Intl J. Heat Mass Transfer* **184**, 122230.
- ROSAS, R.H., ZHANG, Z.P. & WANG, B.C. 2021 Direct numerical simulation of turbulent elliptical pipe flow under system rotation about the major axis. *Phys. Rev. Fluids* **6** (8), 084609.

## *DNS of turbulent pipe flow subjected to axial rotation*

- SMITH, L.M. & WALEFFE, F. 1999 Transfer of energy to two-dimensional large scales in forced, rotating three-dimensional turbulence. *Phys. Fluids* **11** (6), 1608–1622.
- SPEZIALE, C.G., YOUNIS, B.A. & BERGER, S.A. 2000 Analysis and modelling of turbulent flow in an axially rotating pipe. *J. Fluid Mech.* **407**, 1–26.
- STAPLEHURST, P.J. & DAVIDSON, P.A. 2008 Structure formation in homogeneous freely decaying rotating turbulence. *J. Fluid Mech.* **598**, 81–105.
- THIELE, M. & MÜLLER, W.-C. 2009 Structure and decay of rotating homogeneous turbulence. *J. Fluid Mech.* **637**, 425–442.
- WALLIN, S., GRUNDESTAM, O. & JOHANSSON, A.V. 2013 Laminarization mechanisms and extreme-amplitude states in rapidly rotating plane channel flow. *J. Fluid Mech.* **730**, 193–219.
- WELLER, T. & OBERLACK, M. 2006a DNS of a turbulent channel flow with streamwise rotation – investigation on the cross flow phenomena. In *Direct and Large-Eddy Simulation VI* (ed. E. Lamballais, R. Friedrich, B.J. Geurts & O. Métais), pp. 241–248. Springer.
- WELLER, T. & OBERLACK, M. 2006b DNS of a turbulent channel flow with streamwise rotation – study of the reverse effect of the cross flow. *Proc. Appl. Maths. Mech.*, 6(1):553–554.
- WU, H. & KASAGI, N. 2004 Effects of arbitrary directional system rotation on turbulent channel flow. *Phys. Fluids* **16** (4), 979–990.
- WU, X., BALTZER, J.R. & ADRIAN, R.J. 2012 Direct numerical simulation of a 30R long turbulent pipe flow at  $R^+ = 685$ : large- and very large-scale motions. *J. Fluid Mech.* **698**, 235–281.
- WU, X. & MOIN, P. 2008 A direct numerical simulation study on the mean velocity characteristics in turbulent pipe flow. *J. Fluid Mech.* **608**, 81–112.
- WU, X. & MOIN, P. 2009 Direct numerical simulation of turbulence in a nominally zero-pressure-gradient flat-plate boundary layer. *J. Fluid Mech.* **630**, 5–41.
- WU, X., MOIN, P., ADRIAN, R.J. & BALTZER, J.R. 2015 Osborne Reynolds pipe flow: direct simulation from laminar through gradual transition to fully developed turbulence. *Proc. Natl Acad. Sci.* **112** (26), 7920–7924.
- XIA, Z.-H., SHI, Y.-P. & CHEN, S.-Y. 2016 Direct numerical simulation of turbulent channel flow with spanwise rotation. *J. Fluid Mech.* **788**, 42–56.
- YANG, Y.-T., SU, W.-D. & WU, J.-Z. 2010 Helical-wave decomposition and applications to channel turbulence with streamwise rotation. *J. Fluid Mech.* **662**, 91–122.
- YANG, Z., DENG, B.-D., WANG, B.-C. & SHEN, L. 2018 Letter: the effects of streamwise system rotation on pressure fluctuations in a turbulent channel flow. *Phys. Fluids* **30**, 091701.
- YANG, Z. & WANG, B.-C. 2018 Capturing Taylor–Görtler vortices in a streamwise-rotating channel at very high rotation numbers. *J. Fluid Mech.* **838**, 658–689.
- YOSHIMATSU, K., MIDORIKAWA, M. & KANEDA, Y. 2011 Columnar eddy formation in freely decaying homogeneous rotating turbulence. *J. Fluid Mech.* **677**, 154–178.
- YU, C., HU, R., YAN, Z. & LI, X. 2022 Helicity distributions and transfer in turbulent channel flows with streamwise rotation. *J. Fluid Mech.* **940**, A18.
- ZHANG, Z.-P. & WANG, B.-C. 2019 Direct numerical simulation of turbulent flow in a circular pipe subjected to radial system rotation. *Flow Turbul. Combust.* **103** (4), 1057–1079.
- ZHOU, J., ADRIAN, R.J., BALACHANDAR, S. & KENDALL, T.M. 1999 Mechanisms for generating coherent packets of hairpin vortices in channel flow. *J. Fluid Mech.* **387**, 353–396.